

# Coincidences between OVI and OVII Lines: Insights from High Resolution Simulations of the Warm-Hot Intergalactic Medium

Ren Yue Cen<sup>1</sup>

## ABSTRACT

With high resolution ( $0.46h^{-1}\text{kpc}$ ), large-scale, adaptive mesh-refinement Eulerian cosmological hydrodynamic simulations we compute properties of O VI and O VII absorbers from the warm-hot intergalactic medium (WHIM) at  $z = 0$ . Our new simulations are in broad agreement with previous simulations with  $\sim 40\%$  of the intergalactic medium being in the WHIM. Our simulations are in agreement with observed properties of O VI absorbers with respect to the line incidence rate and Doppler width-column density relation. It is found that the amount of gas in the WHIM below and above  $10^6\text{K}$  is roughly equal. Strong O VI absorbers are found to be predominantly collisionally ionized. It is found that (61%, 57%, 39%) of O VI absorbers of  $\log N(\text{OVI}) \text{ cm}^{-2} = (12.5 - 13, 13 - 14, > 14)$  have  $T < 10^5\text{K}$ . Cross correlations between galaxies and strong  $[N(\text{OVI}) > 10^{14}\text{cm}^{-2}]$  O VI absorbers on  $\sim 100 - 300\text{kpc}$  scales are suggested as a potential differentiator between collisional ionization and photoionization models. Quantitative prediction is made for the presence of broad and shallow O VI lines that are largely missed by current observations but will be detectable by COS observations. The reported  $3\sigma$  upper limit on the mean column density of coincidental O VII lines at the location of detected O VI lines by Yao et al. is above our predicted value by a factor of  $2.5 - 4$ . The claimed observational detection of O VII lines by Nicastro et al, if true, is  $2\sigma$  above what our simulations predict.

*Subject headings:* Methods: numerical, absorption lines, Galaxies: evolution, missing baryons, intergalactic medium

## 1. Introduction

Physical understanding of the thermodynamic evolution of the intergalactic medium (IGM) has been substantially improved with the aid of *ab initio* cosmological hydrodynamic simulations. One of the most robust predictions is that 40 – 50% of all baryons in the present universe is in the WHIM of temperature  $10^5 - 10^7\text{K}$  and overdensity  $10 - 300$  (e.g., Cen &

---

<sup>1</sup>Princeton University Observatory, Princeton, NJ 08544; cen@astro.princeton.edu

Ostriker 1999; Davé et al. 2001). The predicted WHIM provides an attractive solution to the long standing missing baryons problem (Persic & Salucci 1992; Fukugita et al. 1998). Let us first clarify the nomenclature of several related gas phases. The intra-group and intra-cluster medium (ICM) is defined to be gas within these virialized regions (i.e., overdensity  $> 100$ ). The high density portion (overdensity  $\geq 500$ ) of the ICM has traditionally been detected in X-ray emission; thermal Sunyaev-Zeldovich effect and more sensitive X-ray measurements can now probe ICM to about the virial radius. The circumgalactic medium (CGM) is usually defined to be gas that embeds the stellar components in galactic halos and may be made up of gases of a wide range of temperatures ( $10^4 - 10^7$ K) and densities. It is likely, at least for large galaxies, that a significant fraction of the CGM falls into the same temperature range of the WHIM. Of particular interest is some of the CGM that has been heated up by star formation feedback shocks to the WHIM temperature range (e.g., Cen & Ostriker 2006; Cen & Chisari 2011). In the present analysis we define WHIM as gas of temperature  $10^5 - 10^7$ K with no density limits. Most of the WHIM gas is truly intergalactic with overdensity  $< 100$  (see Figure 7) and mostly easily probed in absorption.

The reality of the WHIM, at least its low temperature ( $T \leq 10^6$ K) portion, has now been fairly convincingly confirmed by a number of observations in the FUV portion of QSO spectra from HST and FUSE, through the O VI  $\lambda\lambda 1032, 1038$  absorption lines that peak at  $T \sim 3 \times 10^5$ K when collisionally ionized (e.g., Tripp et al. 2000; Tripp & Savage 2000; Oegerle et al. 2000; Savage et al. 2002; Prochaska et al. 2004; Sembach et al. 2004; Danforth & Shull 2005; Danforth et al. 2006; Danforth & Shull 2008; Tripp et al. 2008; Thom & Chen 2008a,b; Cooksey et al. 2008) and Ne VIII  $\lambda\lambda 770, 780$  absorption lines that peak at  $T \sim 7 \times 10^5$ K in collisional ionization equilibrium (Savage et al. 2005, 2006; Narayanan et al. 2009, 2011; Tripp et al. 2011) as well as broad Ly $\alpha$  absorption lines (BLAs) (Danforth et al. 2010; Savage et al. 2011a,b). In agreement with simulations, the part of WHIM detected in O VI absorption is estimated to constitute about 20-30% of total WHIM. The detection of Ne VIII lines along at least some of the sight lines with O VI detection provides unambiguous evidence for the WHIM origin, instead of lower temperature, photoionized gas, under physically plausible and observationally constrained situations.

X-ray observations performed to search for X-ray absorption of the higher temperature portion ( $T \geq 10^6$ K) of the WHIM associated with known massive clusters have also been successful. An XMM-Newton RGS spectrum of quasar LBQS 1228+1116 revealed a feature at the Virgo redshifted position of O VIII Ly $\alpha$  at the 95% confidence level (Fujimoto et al. 2004). Using XMM-Newton RGS observations of an AGN behind the Coma Cluster, the Seyfert 1 X Comae, Takei et al. (2007) claimed to have detected WHIM associated with the Coma cluster. Through the Sculptor Wall Buote et al. (2009) and Fang et al. (2010) have detected WHIM O VII absorption at a column greater than  $10^{16}\text{cm}^{-2}$ . There is evidence of detection in soft X-ray emission along the filament connecting clusters A222 and A223 at  $z = 0.21$  that may be associated with the dense and hot portion of the WHIM (Werner et al.

2008).

However, the search for X-ray absorption of WHIM along random lines of sight turns out to be elusive. Early pioneering observations (Fang et al. 2001, 2002, S5 0836+710, PKS 2149-306, PKS 2155-304) gave the first O VII detection (O VIII for PKS 2155-304), which has not been convincingly confirmed subsequently (Cagnoni et al. 2004; Williams et al. 2007; Fang et al. 2007). Mathur et al. (2003) performed a dedicated deep observation (470 ks) with the Chandra LETGS of the quasar H 1821+643, which has several confirmed intervening O V I absorbers, but found no significant ( $> 2\sigma$ ) X-ray absorption lines at the redshifts of the O V I systems. Nicastro et al. (2005a,b) embarked on a campaign to observe Mrk 421 during its periodic X-ray outbursts with the Chandra LETGS with a total of more than 7 million continuum counts and presented evidence for the detection of two intervening absorption systems at  $z = 0.011$  and  $z = 0.027$ . But the spectrum of the same source observed with the XMM-Newton RGS did not show these absorption lines (Rasmussen et al. 2007), despite higher signal-to-noise and comparable spectral resolution. Kaastra et al. (2006) and Yao et al. (2012) reanalyzed the Chandra LETGS data and were in agreement with Rasmussen et al. (2007). The detection of O VII lines may also be at odds with recent BLA measurements (Danforth et al. 2011), under simplistic assumptions about the nature of the absorbing medium. However, it has been argued that the reported XMM-Newton upper limits and the Chandra measurements may be consistent with one another, when taking into consideration certain instrumental characteristics of the XMM-Newton GRS (Williams et al. 2006). Moreover, an analysis of the two candidate X-ray absorbers at  $z = 0.011$  and  $z = 0.027$  yields intriguing evidence of two large-scale filaments at the respective redshifts, one of which has only 5 – 10% probability of occurring by chance (Williams et al. 2010). Observations of 1ES 1028+511 at  $z = 0.361$  by Steenbrugge et al. (2006) yield no convincing evidence for X-ray WHIM absorption.

What is perceived to be more disconcerting is the lack of detection of O VII absorbers at the redshifts of detected O VI absorbers along some random lines of sight. This is because, overall, the O VII line is predicted to be the most abundant and anecdotal evidence suggests substantial coincidence between O VI and O VII (e.g., Cen & Fang 2006). A statistically significant upper limit placed on the mean column density of O VII absorbers at the locations of a sizeable set of detected O VI absorbers using stacking techniques by Yao et al. (2009) prompts them to call into question the very existence of the high temperature ( $T \geq 10^6\text{K}$ ) portion of the WHIM, although the limited sensitivity and spectral resolution of the current X-ray observations may render any such conclusions less than definite.

Therefore, at this juncture, it is pressing to statistically address this lack of significant coincidence between O VI and O VII absorbers and other issues theoretically, through higher resolution simulations that are necessary in order to well resolve the interfaces of multi-phase media. This is the primary purpose of this paper. We use two simulations of high resolution

of  $0.46h^{-1}\text{kpc}$  and box size of  $20 - 30h^{-1}\text{Mpc}$  to perform much more detailed characterization of O VI and O VII lines to properly compare to extant observations. This high resolution is to be compared with  $83h^{-1}\text{kpc}$  resolution in our previous simulations (Cen & Ostriker 2006; Cen & Fang 2006),  $25 - 49h^{-1}\text{kpc}$  resolution in Smith et al. (2011) and Shull et al. (2011),  $1.25 - 2.5h^{-1}\text{kpc}$  in Oppenheimer et al. (2012) and  $1.25 - 2.5h^{-1}\text{kpc}$  in Tepper-García et al. (2011), resolves the Jeans scale of WHIM by 2-3 orders of magnitude and interfaces between gas phases of different temperatures in a multi-phase medium. It is useful to distinguish, in the case of SPH simulations, between the gravity force resolution and the resolution of the hydrodynamics solver, with the latter being worse than the former by a factor of order a few. It is also useful to keep in mind the initial cell size or interparticle separation, because in both SPH and adaptive mesh refinement (AMR) simulations not all regions are resolved by the maximum resolution. Calling this “mean region resolution”  $\Delta_{\text{root}}$ ,  $\Delta_{\text{root}} = (117, 25 - 49, 125, 195)h^{-1}\text{kpc}$  for [this paper, Smith et al. (2011), Oppenheimer et al. (2012), Tepper-García et al. (2011)]. We note that a region of overdensity  $\delta$  is approximately resolved at a resolution of  $C\Delta_{\text{root}}\delta^{-1/3}$  (up to a pre-specified highest resolution), where the pre-factor  $C$  is about unity for AMR simulations and  $\sim 2$  for SPH simulations. Using Lagrangian SPH or AMR approaches becomes necessary for regions  $\delta \geq 300$ , because simulations of a similar resolution with the uni-grid method become increasingly impractical (largely due to limitations of computer memory). A more important advantage with very high resolution simulations has to do with the need to resolve galaxies, which in turn allows for a more self-consistent treatment of the feedback processes from star formation, namely, the temporal and spatial distribution of metals and energy deposition rates to the CGM and IGM and their effects on subsequent star formation.

Our new simulations, in agreement with earlier findings, reaffirm quantitatively the existence of WHIM and furthermore show that the properties of the WHIM with respect to O VI line and O VI-O VII relations are fully consistent with observations. In particular, the observed upper limit of the mean coincidental O VII column density of detected O VI absorbers is higher than what is predicted by the simulations by a factor of  $\sim 2.5 - 4$ . Higher sensitivity X-ray observations or a larger sample by a factor of  $\sim 10$  should test this prediction definitively. The outline of this paper is as follows. In §2.1 we detail simulation parameters and hydrodynamics code, followed by a description of our method of making synthetic O VI and O VII spectra in §2.2, which is followed by a description of how we average the two separate simulations C (cluster) and V (void) run in §2.3. Results are presented in §3. In §3.1 we present some observables for O VI to compare to observations to provide additional validation of the simulations. In §3.2 we dissect the simulations to provide a physical analysis of the O VI and O VII absorbers. In §3.3 results on the coincidences between O VI and O VII lines are given. Conclusions are summarized in §4.

## 2. Simulations

### 2.1. Hydrocode and Simulation Parameters

We perform cosmological simulations with the AMR Eulerian hydro code, Enzo (Bryan 1999; Bryan & Norman 1999; O’Shea et al. 2005; Joung et al. 2009). First we ran a low resolution simulation with a periodic box of  $120 h^{-1}\text{Mpc}$  on a side. We identified two regions separately, one centered on a cluster of mass of  $\sim 2 \times 10^{14} M_{\odot}$  and the other centered on a void region at  $z = 0$ . We then resimulate each of the two regions separately with high resolution, but embedded in the outer  $120 h^{-1}\text{Mpc}$  box to properly take into account large-scale tidal field and appropriate boundary conditions at the surface of the refined region. We name the simulation centered on the cluster “C” run and the one centered on the void “V” run. The refined region for “C” run has a size of  $21 \times 24 \times 20 h^{-3}\text{Mpc}^3$  and that for “V” run is  $31 \times 31 \times 35 h^{-3}\text{Mpc}^3$ . At their respective volumes, they represent  $1.8\sigma$  and  $-1.0\sigma$  fluctuations. **The root grid has a size of  $128^3$  with  $128^3$  dark matter particles. The initial static grids in the two refined boxes correspond to a  $1024^3$  grid on the outer box. The initial number of dark matter particles in the two refined boxes correspond to  $1024^3$  particles on the outer box. This translates to initial condition in the refined region having a mean interparticle-separation of  $117 h^{-1}\text{kpc}$  comoving and dark matter particle mass of  $1.07 \times 10^8 h^{-1} M_{\odot}$ .** The refined region is surrounded by two layers (each of  $\sim 1 h^{-1}\text{Mpc}$ ) of buffer zones with particle masses successively larger by a factor of 8 for each layer, which then connects with the outer root grid that has a dark matter particle mass  $8^3$  times that in the refined region. The initial density fluctuations are included up to the Nyquist frequency in the refined region. The surrounding volume outside the refined region is also followed hydrodynamically, which is important in order to properly capture matter and energy exchanges at the boundaries of the refined region. Because we still can not run a very large volume simulation with adequate resolution and physics, we choose these two runs of moderate volumes to represent two opposite environments that possibly bracket the average.

We choose the mesh refinement criterion such that the resolution is always better than  $460 h^{-1}\text{pc}$  physical, corresponding to a maximum mesh refinement level of 11 at  $z = 0$ . The simulations include a metagalactic UV background (Haardt & Madau 2012), and a model for shielding of UV radiation by neutral hydrogen (Cen et al. 2005). The simulations also include metallicity-dependent radiative cooling and heating (Cen et al. 1995). We clarify that our group has included metal cooling and metal heating (due to photoionization of metals) in all our studies since Cen et al. (1995), contrary to some claims (e.g., Wiersma et al. 2009; Tepper-García et al. 2011). Star particles are created in cells that satisfy a set of criteria for star formation proposed by Cen & Ostriker (1992). Each star particle is tagged with its initial mass, creation time, and metallicity; star particles typically have masses of  $\sim 10^6 M_{\odot}$ .

Supernova feedback from star formation is modeled following Cen et al. (2005). Feedback energy and ejected metal-enriched mass are distributed into 27 local gas cells centered at the star particle in question, weighted by the specific volume of each cell (i.e., weighting is equal to the inverse of density), which is to mimic the physical process of supernova blastwave propagation that tends to channel energy, momentum and mass into the least dense regions (with the least resistance and cooling). We allow the whole feedback processes to be hydrodynamically coupled to surroundings and subject to relevant physical processes, such as cooling and heating, as in nature. The extremely inhomogeneous metal enrichment process demands that both metals and energy (and momentum) are correctly modeled so that they are transported into right directions in a physically sound (albeit still approximate at the current resolution) way, at least in a statistical sense.

The primary advantages of this supernova energy based feedback mechanism are three-fold. First, nature does drive winds in this way and energy input is realistic. Second, it has only one free parameter  $e_{SN}$ , namely, the fraction of the rest mass energy of stars formed that is deposited as thermal energy on the cell scale at the location of supernovae. Third, the processes are treated physically, obeying their respective conservation laws (where they apply), allowing transport of metals, mass, energy and momentum to be treated self-consistently and taking into account relevant heating/cooling processes at all times. We use  $e_{SN} = 1 \times 10^{-5}$  in these simulations. The total amount of explosion kinetic energy from Type II supernovae with a Chabrier IMF translates to  $e_{SN} = 6.6 \times 10^{-6}$ . Observations of local starburst galaxies indicate that nearly all of the star formation produced kinetic energy (due to Type II supernovae) is used to power galactic superwinds (e.g., Heckman 2001). Given the uncertainties on the evolution of IMF with redshift (i.e., possibly more top heavy at higher redshift) and the fact that newly discovered prompt Type I supernovae contribute a comparable amount of energy compared to Type II supernovae, it seems that our adopted value for  $e_{SN}$  is consistent with observations and within physical plausibility. Test of the success of this feedback approach comes empirically. As we show in Cen (2012), the metal distribution in and around galaxies over a wide range of redshift is in good agreement with respect to the properties of observed damped Ly $\alpha$  systems; this is a non-trivial success and provides strong validation of the simulations. We will provide additional validation of the simulations in §3.1.

To better understand differences in results between AMR and SPH simulations that we will discuss later, we note here that the evolution of metals in the two types of simulations is treated rather differently. In AMR simulations metals are followed hydrodynamically by solving the metal density continuity equation with sources (from star formation feedback) and sinks (due to subsequent star formation), whereas in SPH simulations of WHIM one does not separately solve the metal density continuity equation. Thus, metal mixing and diffusion through advection, turbulence and other hydrodynamic processes are properly captured in AMR simulations. While some SPH simulations have implemented metal diffusion schemes

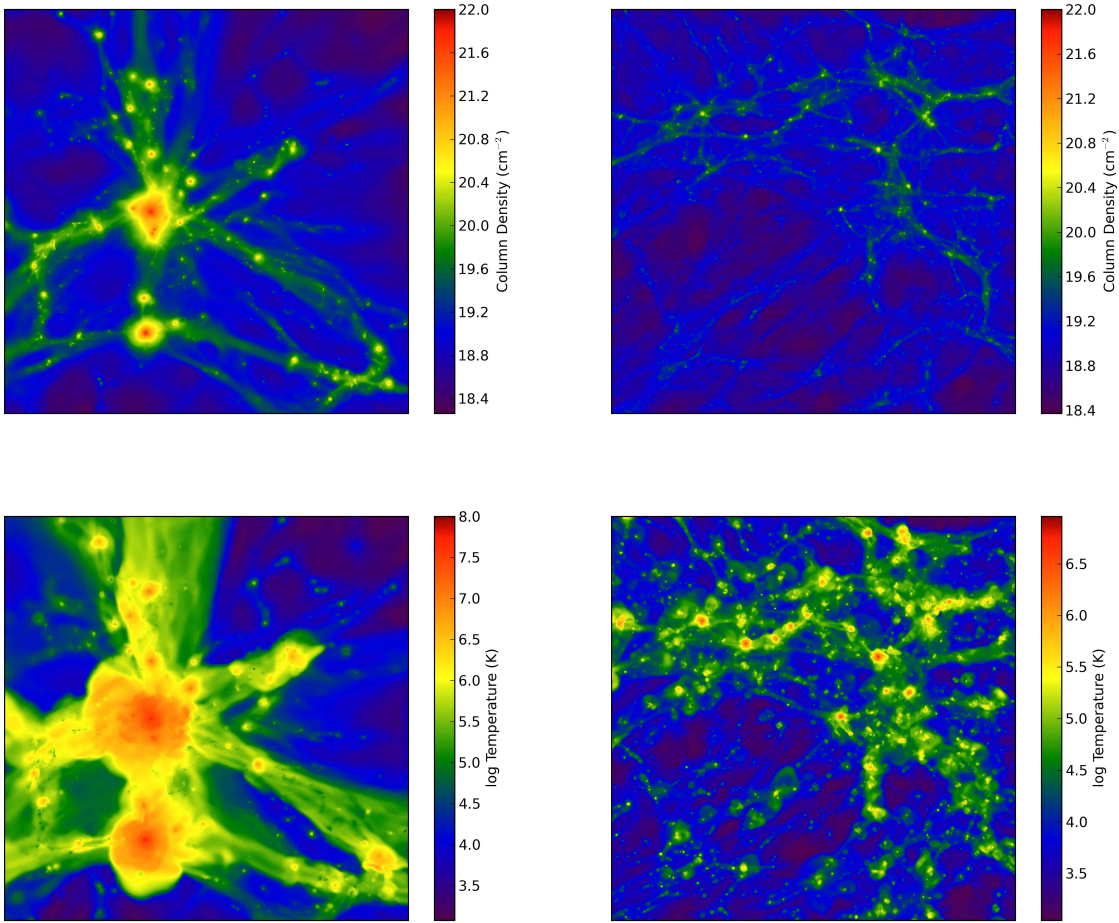


Fig. 1.— Top-left and bottom-left panels show the gas density and density-weighted temperature projection of a portion of the refinement box of the C run of size  $(18h^{-1}\text{Mpc})^3$ . Top-right and bottom-right panels show the gas density and density-weighted temperature projection of a portion of the refinement box of the V run of size  $(30h^{-1}\text{Mpc})^3$ .

that are motivated by some subgrid turbulence model as a remedy parameterized to roughly match results from hydrodynamic simulations (e.g., Shen et al. 2010), most SPH simulations of WHIM obtain gas metallicities based on kernel-smoothed metal masses of feedback SPH particles that are assigned at birth and un-evolved (e.g., Tepper-García et al. 2011; Oppenheimer & Davé 2009; Oppenheimer et al. 2012). In the simulations of Oppenheimer et al. (2012) “feedback” SPH particles with initially given metal masses are launched (in random directions) to be transported ballistically to sufficiently large distance ( $\sim 10\text{kpc}$ ), after allowance for some period of hydrodynamic de-coupling between the feedback SPH particles and other neighboring SPH particles. Once some of the feedback parameters are fixed, this approach produces definitive predictions with respect to various aspects of stellar and IGM

metallicity and others (e.g., Springel & Hernquist 2003; Oppenheimer & Davé 2009; Tornatore et al. 2010; Davé et al. 2011b,a; Oppenheimer et al. 2012). It is likely that mixing of metals on small to intermediate scales ( $\sim 1-100\text{kpc}$ ) in SPH simulations (e.g., Oppenheimer et al. 2012; Tepper-García et al. 2011) is probably substantially underestimated. This significant difference in the treatment of metal evolution may have contributed, in a large part, to some discrepancies between SPH and AMR hydrodynamic simulations, as we will discuss later.

We use the following cosmological parameters that are consistent with the WMAP7-normalized (Komatsu et al. 2010) LCDM model:  $\Omega_M = 0.28$ ,  $\Omega_b = 0.046$ ,  $\Omega_\Lambda = 0.72$ ,  $\sigma_8 = 0.82$ ,  $H_0 = 100h\text{kms}^{-1}\text{Mpc}^{-1} = 70\text{kms}^{-1}\text{Mpc}^{-1}$  and  $n = 0.96$ .

Figure 1 shows the density and temperature fields of the two simulations. The environmental contrast between the two simulations is evident. We also note that there is substantial overlap visually between the two simulations in that both cover the “field” environment, which we have shown quantitatively in Tonnesen & Cen (2011). In other words, these two simulations cover two extreme environments - voids and clusters - with substantial overlap of intermediate environment that facilitates possible averaging of some computed quantities, with proper normalizations by independent observational constraints.

## 2.2. Generation of Synthetic O VI and O VII Absorption Lines

The photoionization code CLOUDY (Ferland et al. 1998) is used post-simulation to compute the abundance of O VI and O VII, adopting the shape of the UV background calculated by Haardt & Madau (2012) normalized by the intensity at 1 Ryd determined by Shull et al. (1999) and assuming ionization equilibrium.

We generate synthetic absorption spectra using a code similar to that used in our earlier papers (e.g., Cen et al. 1994, 2001; Cen & Fang 2006), given the density, temperature, metallicity and velocity fields from simulations. Each absorption line is identified by the interval between one downward and the next upward crossing in the synthetic flux spectrum without noise at a flux equal to 0.99 (flux equal to unity corresponds to an unabsorbed continuum). Since the absorption lines in question are sparsely distributed in velocity space, their identifications have no significant ambiguity. Column density, equivalent width, Doppler width, mean column density weighted velocity and physical space locations, mean column density weighted temperature, density and metallicity are computed for each line. We sample the C and V run, respectively, with 72,000 and 168,000 random lines of sight at  $z = 0$ , with a total pathlength of  $\Delta z \sim 2000$ . While a detailed Voigt profile fitting of the flux spectrum would have enabled closer comparisons with observations, simulations suggest that such an exercise does not necessarily provide a more clarifying physical understanding of



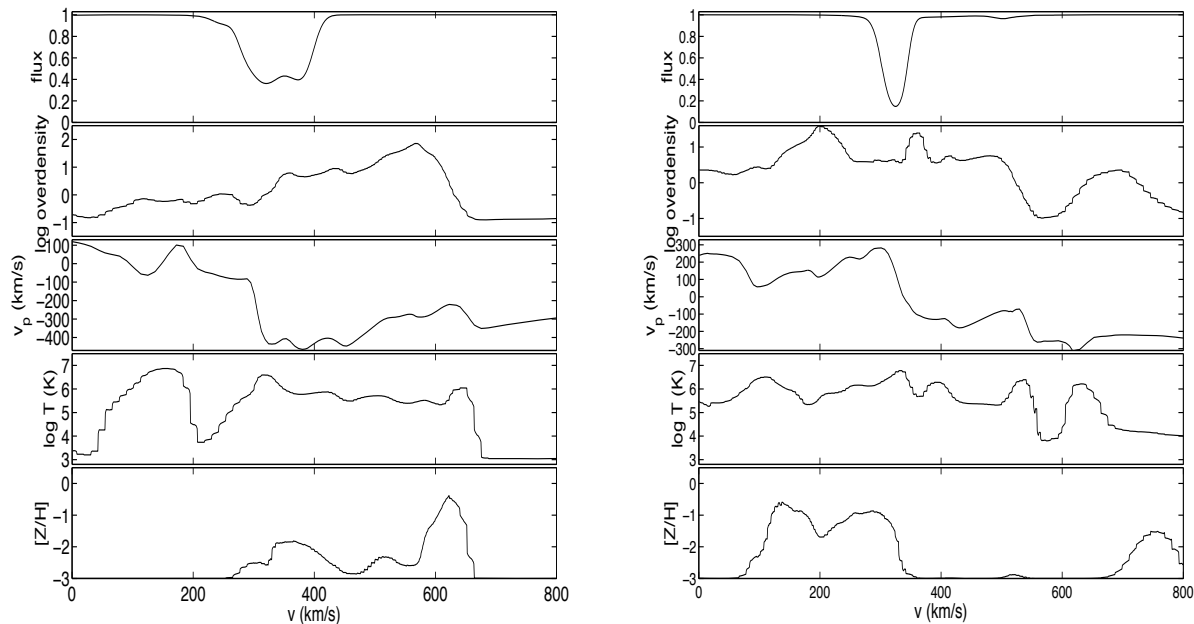


Fig. 2.— shows flux spectra of two separate O VI lines and physical conditions. The left and right cases have column densities of  $\log N(\text{OVI})\text{cm}^2 = 14.48$  and  $14.30$ , respectively. The five panels from top to bottom are: flux, gas overdensity, proper peculiar velocity, temperature and metallicity in solar units. While the x-axis for the top panel is the Hubble velocity, the x-axis for the bottom four panels is physical distance that is multiplied by the Hubble constant.

the absorber properties, because bulk velocities are very important (see Figure 6 below) and velocity substructures within an absorber do not necessarily correspond to separate physical entities.

A small number of simulated spectra may not serve to illustrate the extreme rich and complex physics involved. It may even be misleading in the sense that any statistical conclusions drawn based on anecdotal evidence could be substantially wrong. Thus, we will present two absorption spectrum segments merely only for the purpose of illustration. Figure 2 shows two O VI lines and their associated physical environment.

### 2.3. Averaging C and V Runs

The C and V runs at  $z = 0$  are used to obtain an “average” of the universe. This cannot be done precisely without much larger simulation volumes, which is presently not feasible. Nevertheless, it is still possible to obtain an approximate average. Since the WHIM is mostly closely associated with groups and clusters of galaxies, we will use X-ray clusters

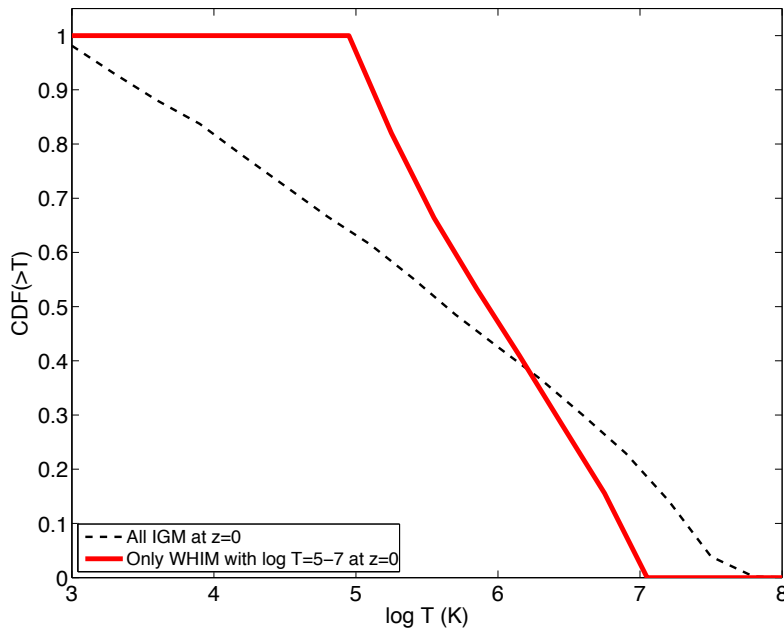


Fig. 3.— shows the cumulative probability distribution function (CDF) of the IGM at  $z = 0$  as a function of gas temperature (black dashed curve) and that of the WHIM only in the temperature range  $T = 10^5 - 10^7$  K (red solid curve); stars are not included.

as an appropriate “normalization” anchor point. We normalize averaging weightings of the C and V runs by requiring that the fraction of hot gas with temperature  $T \geq 10^7$  K is consistent with the observed value of  $\sim 15\%$  of baryons at  $z = 0$  (Bahcall 2011). Note that small variations on the adopted X-ray gas fraction do not cause large changes in most of the results. For comparative measures such as the coincidence rates between O VI and O VII absorbers, the dependence on the normalization procedure is still weaker. The results are shown in Figure 3, which shows the temperature distribution of entire IGM and WHIM at  $z = 0$ . In agreement with previous simulations (e.g., Cen & Ostriker 1999; Davé et al. 2001; Cen & Ostriker 2006), we find that  $\sim 40\%$  of the IGM at  $z = 0$  is in WHIM. This is compared to 35-40% in Smith et al. (2011), 24% in Davé et al. (2010) (limited to overdensities outside halos), 40% in Shen et al. (2010) and 40% and 50% in Tornatore et al. (2010) in their wind and black hole feedback models, respectively. In simulations of Cen et al. (1995); Cen & Ostriker (1999); Cen et al. (2001); Cen & Ostriker (2006); Cen & Chisari (2011), Wiersma et al. (2009); Tepper-García et al. (2011), Shen et al. (2010) and Shull et al. (2011), in addition to radiative processes of a primordial gas, both metal cooling (due to collisional excitation and recombination) and metal heating (due to photo-ionization heating of metal species) in the presence of UV-X-ray background are included, whereas in Oppenheimer & Davé (2009), Oppenheimer et al. (2012) and Tornatore et al. (2010) only metal cooling is included. Tepper-García et al. (2011) suggest that the relatively overall low fraction of

WHIM in the latter (25%) versus higher fraction in the former (35-50%) may be accounted by the difference in the treatment of metal heating; we concur with their explanation for at least part of the difference. All these simulations have a box size of  $\sim 50h^{-1}\text{Mpc}$ , which still suffers from significant cosmic variance: Davé et al. (2001) show that WHIM fraction increases from 37% to 42% from a box size of  $50h^{-1}\text{Mpc}$  to  $100h^{-1}\text{Mpc}$  in two Eulerian simulations. The amplitude of power spectrum has a similar effect and may be able to, at least in part, account for some of the differences among the simulations;  $\sigma_8 = (0.82, 0.82, 0.74, 0.77, 0.80, 0.82)$  in [this work, Shull et al. (2011), Tepper-García et al. (2011), Shen et al. (2010), Tornatore et al. (2010), Oppenheimer et al. (2012)]. Gravitational collapse of longer waves powers heating of the IGM at later times. We suggest that the peak of WHIM fraction at  $z \sim 0.5$  found in the  $25h^{-1}\text{Mpc}$  simulation boxes in Smith et al. (2011) is because of the small box size; in other words, available, reduced gravitational heat input in the absence of breaking density waves of lengths longer than  $25h^{-1}\text{Mpc}$  at  $z \leq 0.5$  fails to balance the cooling due to (primarily) universal expansion and (in part) radiative cooling. This explanation is supported by the behavior of their simulation boxes of size  $50h^{-1}\text{Mpc}$  at low redshift ( $z \leq 0.5$ ). Figure 3 shows that within the WHIM temperature range, roughly equal amounts are at  $T = 10^5 - 10^6\text{K}$  and  $T = 10^6 - 10^7\text{K}$ .

### 3. Results

#### 3.1. Simulation Validation with Properties of O VI Absorbers

The present simulations have been shown to produce the metal distribution in and around galaxies over a wide range of redshift ( $z = 0 - 4$ ) that is in good agreement with respect to the properties of observed damped  $\text{Ly}\alpha$  systems (Cen 2012). Here we provide additional, more pertinent validation with respect to O VI absorbers in the IGM at  $z = 0$ . The top panel of Figure 4 shows a scatter plot of simulated O VI absorbers (red pluses) in the Doppler width ( $b$ )-O VI column density [ $N(\text{OVI})$ ] plane, compared to observations. The agreement is excellent in that the observed O VI absorbers occupy a region that overlaps with the simulated one. It is intriguing to note that the simulations predict a large number of large  $b$ , low  $N(\text{OVI})$  (i.e., broad and shallow) absorbers in the region  $b > 31(N(\text{OVI})/10^{14}\text{cm}^{-2})^{0.4}\text{km/s}$ , corresponding to the upper left corner to the green dashed line, where there is no observed O VI absorber. This green dashed line, however, has no physical meaning to the best of our knowledge. The blue solid line of unity logarithmic slope has a clear physical origin, which is a requirement for the decrement at the flux trough of the weaker of the O VI doublet to be 4%:  $b = 25(N(\text{OVI})/10^{13}\text{cm}^{-2})\text{km/s}$ . Current observational data are heterogeneous with varying qualities. Thus, the blue solid line is a much simplified characterization of the complex situation. Nevertheless, one could understand the desert of observed O VI absorbers in the upper left corner to the blue solid line, thanks to the difficulty of identifying broad

and shallow lines in existing observations. We attribute the “missing” observed O VI lines in the upper right corner between the blue solid line and the green dashed line, in part, to the observational procedure of Voigt profile fitting that may break up some large  $b$  lines into separate, narrower components, whereas no such procedure is performed in the presented simulation results.

Ongoing and upcoming observations by the Cosmic Origins Spectrograph (COS) (e.g., Froning & Green 2009; Shull 2009; Green et al. 2012) will be able to substantially improve in sensitivity and thus likely be able to detect a sizeable number of O VI lines in the upper left corner to the blue solid line. Quantitative distribution functions of  $b$  parameter will be shown in Figure 10 later, for which COS may provide a strong test. The bottom panel of Figure 4 shows a scatter plot of simulated O VII absorbers (red pluses); because there is no data to compare to, we only note that the positive correlation between  $b$  and  $N(\text{OVI})$  is stronger for O VII lines than for O VI lines, in part due to less important contribution to the O VII lines from photoionization and in part due to positive correlation between density and velocity dispersion.

Figure 5 shows O VI line density as a function of column density. The agreement between simulations and observations of Danforth & Shull (2008) is excellent over the entire column density,  $N(\text{OVI}) \sim 10^{13} - 10^{15} \text{cm}^{-2}$ , where comparison can be made. The simulation results are up to a factor of  $\sim 2$  below the observational results of Tripp et al. (2008) in the column density range  $N(\text{OVI}) \sim 10^{13.7} - 10^{14.5} \text{cm}^{-2}$ . Some of the disagreement is due to different treatments in defining lines in that we do not perform Voigt profile fitting thus deblending of non-gaussian profiles into multiple components, where the observational groups do and different groups often impose different, subjective criteria of choosing the “goodness” of the fit. The down turn of line density towards lower column densities from  $N(\text{OVI}) \sim 10^{13.9} \text{cm}^{-2}$  from Tripp et al. (2008) as well as the lower values in the column density range  $N(\text{OVI}) \sim 10^{13.2} - 10^{13.7} \text{cm}^{-2}$  of Danforth & Shull (2008) may be related to the “missing” broad and shallow lines, as indicated in the top panel of Figure 4. It is noted that the observed line density at  $N(\text{OVI}) \sim 10^{13} \text{cm}^{-2}$  of the Danforth & Shull (2008) data displays an upturn and lies on top of the simulated curve. Closer examination reveals that this is due to the presence of two relatively broad absorbers at  $N(\text{OVI}) \sim 10^{13} \text{cm}^{-2}$  and  $b \sim 30 \text{ km/s}$ . We expect that the upcoming COS observations will substantially raise the line density at  $N(\text{OVI}) \leq 10^{13.5} \text{cm}^{-2}$ .

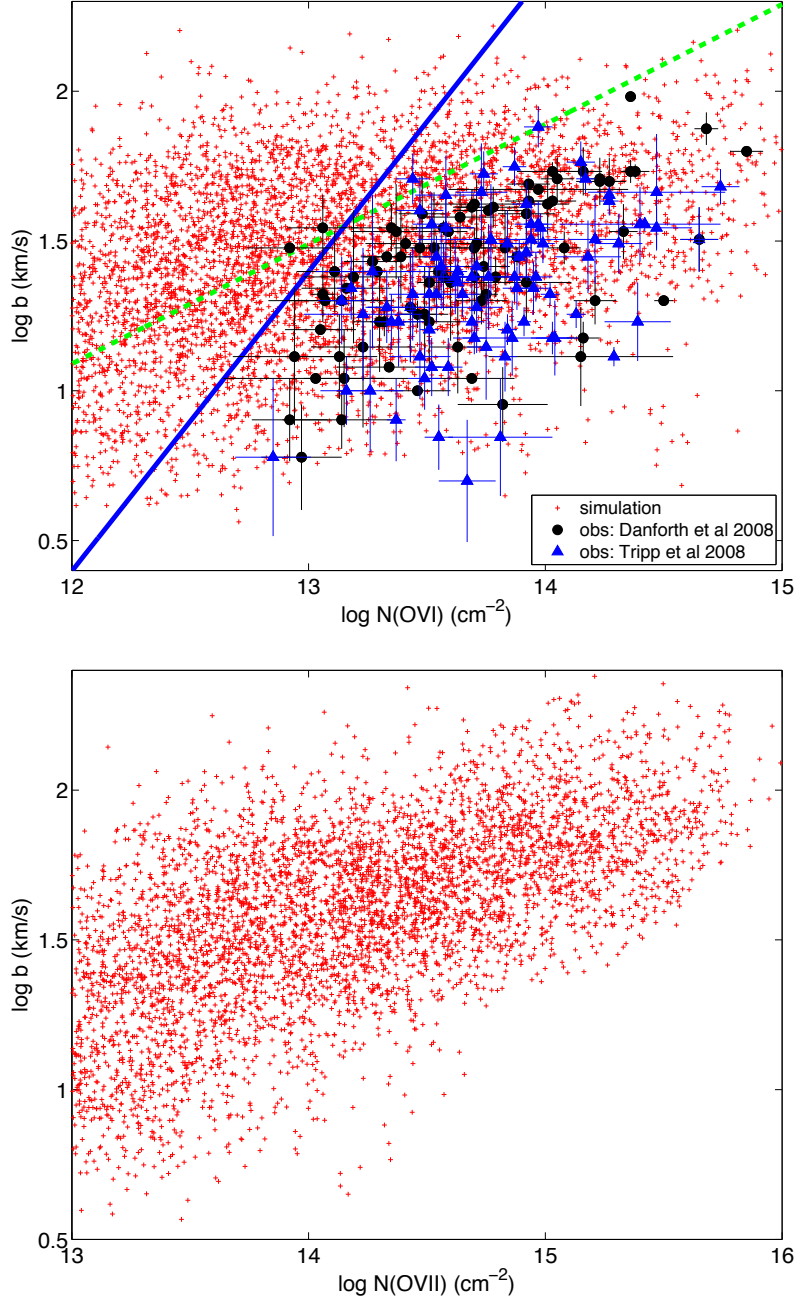


Fig. 4.— Top panel shows a scatter plot of simulated O VI absorbers (red pluses) in the  $b$ - $N(\text{OVI})$  plane. Also shown as black dots and blue triangles are the observations from Danforth & Shull (2008) and Tripp et al. (2008), respectively. The green dashed line of slope 4/10 is only intended to guide the eye to suggest that there appears to be a desert of observed O VI absorbers in the upper left corner. The blue solid line of unity logarithmic slope is a requirement for the decrement at the flux trough of the weaker of the O VI doublet to be 4%:  $b = 25(N(\text{OVI})/10^{13}\text{cm}^{-2})\text{km/s}$ . Bottom panel shows the same for the O VII absorbers.

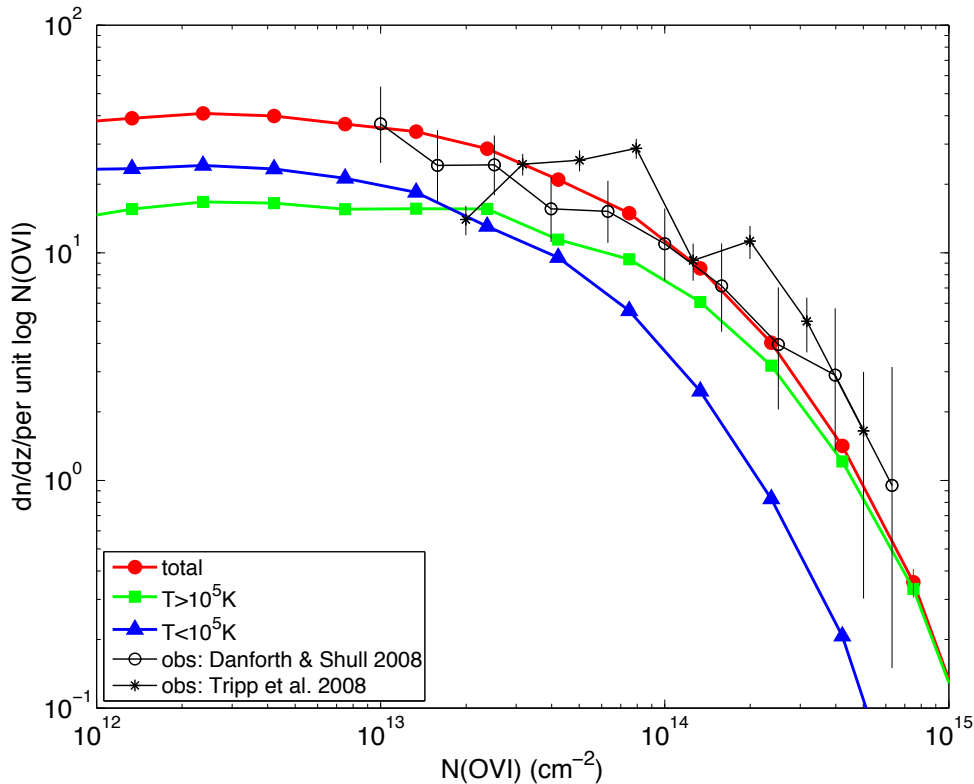


Fig. 5.— shows the O VI line density as a function of column density, defined to be the number of lines per unit redshift per unit logarithmic interval of the column density. The red solid dots, green squares and blue triangles are the total, collisionally ionized and photoionized absorbers, respectively. Also shown as black open circles and stars are the observations from Danforth & Shull (2008) and Tripp et al. (2008), respectively.

These results show that our simulation results are realistic with respect to the abundance of O VI lines in the CGM and IGM. This is a substantial validation of the simulations, when considered in conjunction with the success of the simulations with respect to the damped Ly $\alpha$  systems (Cen 2012). The damped Ly $\alpha$  systems primarily originate in gas within the virial radii of galaxies, whereas the O VI absorbers examined here extend well into the IGM, some reaching as far as the mean density of the universe (see Figure 7 below). In combination, they require the simulations to have substantially correctly modeled the propagation of initial metal-enriched blastwaves from sub-kpc scales to hundreds of kiloparsecs as well as other complex thermodynamics, at least in a statistical sense. Since O VII absorbers arise in regions in-between, this gives us confidence that O VII lines are also modeled correctly and the comparisons that we will make between O VI and O VII lines are meaningful.

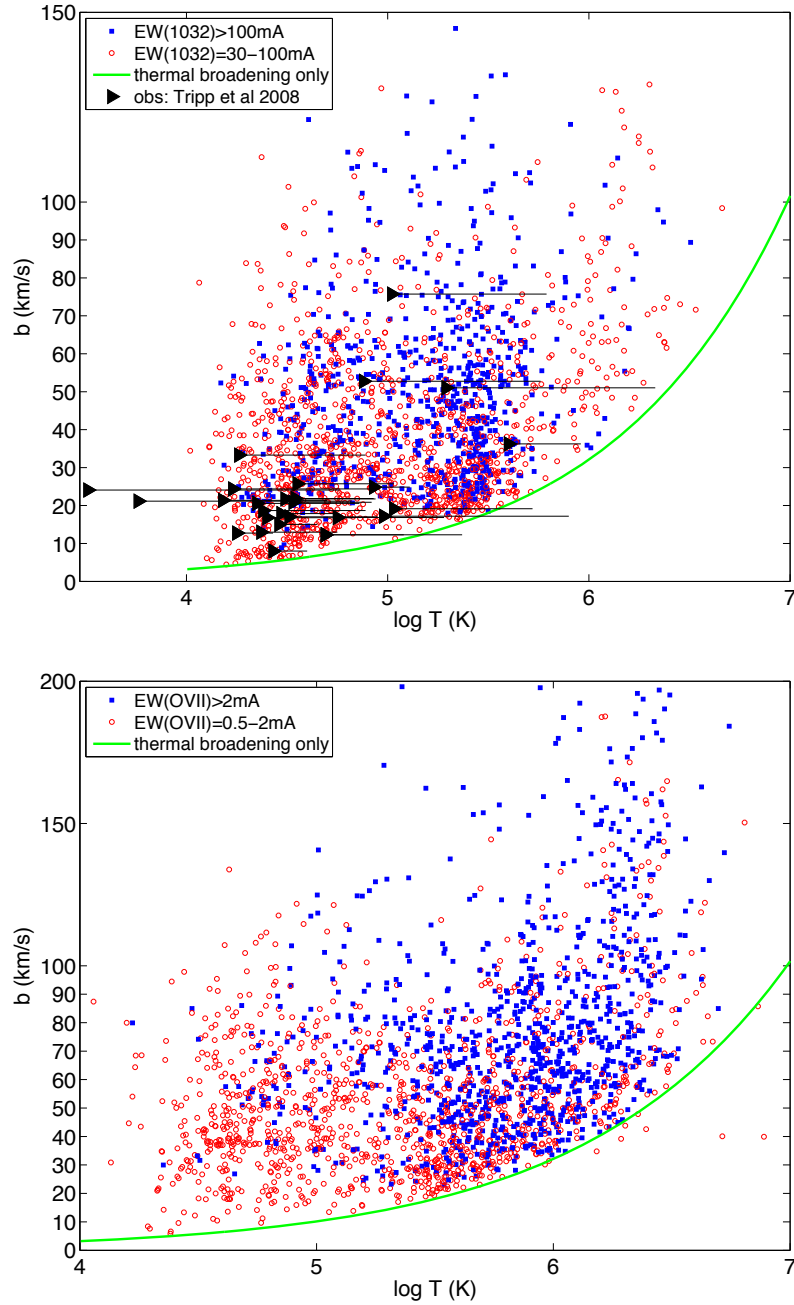


Fig. 6.— shows absorbers in the  $b$ – $T$  plane for O VI line (top panel) and O VII line (bottom panel). Within each panel, we have broken up the absorbers into strong ones (blue squares) and weak ones (red circles). Only thermally broadened lines should follow the indicated solid green curve (Eq. 1). Also shown as right-pointing triangles are observed data of Tripp et al. (2008) based on a joint analysis of  $\text{Ly}\alpha$  and O VI lines; the location of each triangle is the best estimate of the temperature and the rightmost tip of the attached line to each triangle represents a  $3\sigma$  upper limit.

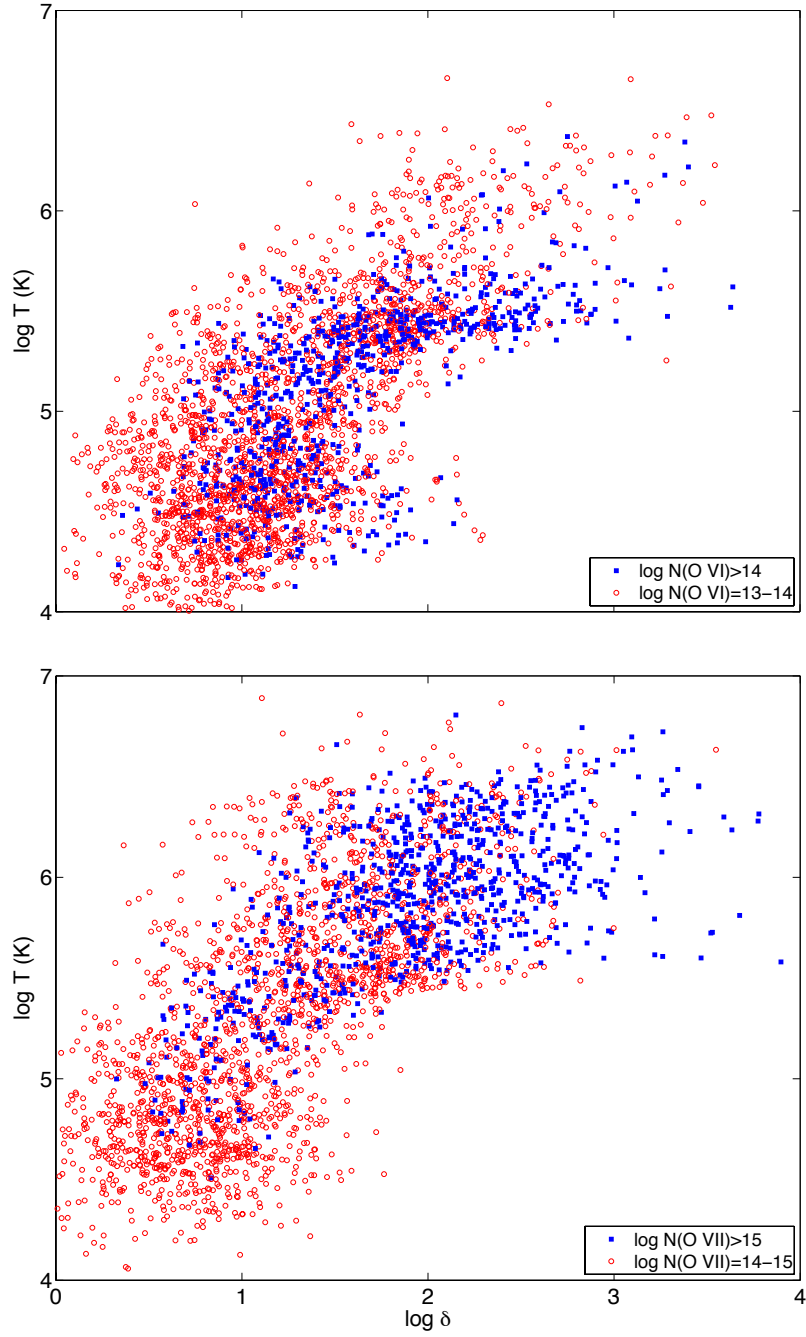


Fig. 7.— shows absorbers in the temperature-density plane for O VI line (top panel) and O VII line (bottom panel). Within each panel, we have broken up the absorbers into strong ones (blue squares) and weak ones (red circles).



### 3.2. Physical Properties of O VI and O VII Lines

In this subsection we will present physical properties of both O VI and O VII absorbers and relationships between them. For most of the figures below we will show results in pairs, one for O VI and the other for O VII, to facilitate comparisons.

Figure 6 shows absorbers in the  $b - T$  plane for O VI (top panel) and O VII absorbers (bottom panel). For thermal broadening only absorbers the  $b - T$  relation would follow the solid green curve obeying this formula:

$$b(O) = 10.16(T/10^5\text{K})^{1/2} \text{ km/s.} \quad (1)$$

It is abundantly clear from Figure 6 that  $b$  is a poor indicator of absorber gas temperature. Bulk velocity structures within each absorbing line are important. For O VI lines of equivalent width greater than 100mÅ, it appears that bulk velocity structures are dominant over thermal broadening at all temperatures. No line is seen to lie below the green curve, as expected. All of the observationally derived temperature limits shown, based on a joint analysis of line profiles of well-matched coincidental Ly $\alpha$  and O VI lines by Tripp et al. (2008), are seen to be fully consistent with our simulation results. It is noted that velocity structures in unvirialized regions typically do not have gaussian distributions (in 1-d). Caustic-like velocity structures are frequently seen that are reminiscent of structure collapse along one dimension (e.g., Zeldovich pancake or filaments); for anecdotal evidence see Figure 2. Thus, we caution that temperatures derived on the grounds of gaussian velocity profile (e.g., Tripp et al. 2008) may be uncertain. A more detailed analysis will be performed elsewhere. The situations with respect to O VII absorbers are similar to O VI absorbers.

Figure 7 shows absorbers in the temperature-density plane for O VI (top panel) and O VII absorbers (bottom panel). In the top panel we see that strong O VI absorbers with  $N(\text{OVI}) \geq 10^{14} \text{ cm}^{-2}$  have a large concentration at  $(\delta, T) = (10 - 300, \sim 10^{5.5} \text{ K})$  that corresponds to collisional ionization dominated O VI population, consistent with Figure 5. For weaker absorbers with  $N(\text{OVI}) = 10^{13-14} \text{ cm}^{-2}$  we see that those with temperature above and those below  $10^5 \text{ K}$  are roughly equal, consistent with Figure 5; the density distributions for the two subsets are rather different: for the lower-temperature ( $T < 10^5 \text{ K}$ ) subset the gas density is concentrated around  $\delta \sim 10$  that is photoionization dominated, whereas for the higher-temperature ( $T > 10^5 \text{ K}$ ) subset the gas density is substantially spread out over  $\delta \sim 3 - 3000$ , which are mostly collisional ionization dominated. Finally, we note that still weaker lines with  $N(\text{OVI}) < 10^{13} \text{ cm}^{-2}$ , not shown here, are mostly photoionization dominated, as indicated in Figure 5. In the bottom panel we see that strong O VII absorbers with  $N(\text{OVII}) \geq 10^{15} \text{ cm}^{-2}$  are predominantly collisionally ionized at  $T \sim 10^{5.5} - 10^{6.5} \text{ K}$  and  $\delta \sim 10 - 1000$ , with a small fraction of lines concentrated at an overdensity of  $\sim 3 - 20$  and temperatures below  $10^{5.5} \text{ K}$ . For weaker absorbers with  $N(\text{OVII}) = 10^{14-15} \text{ cm}^{-2}$  collisionally ionized ones at temperatures greater than  $10^{5.5} \text{ K}$  and those photoionized at lower temperatures are roughly

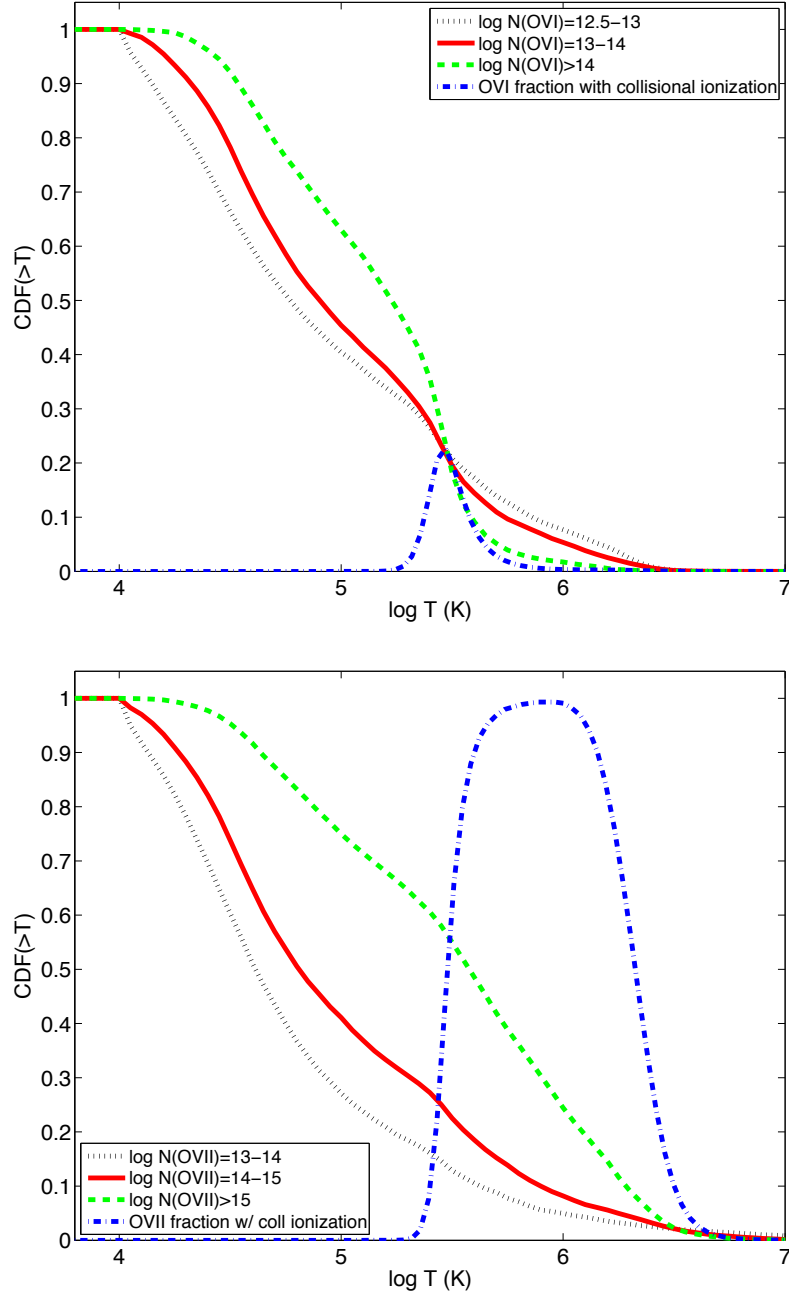


Fig. 8.— shows the cumulative probability distribution functions as a function of absorber temperature for three subsets of O VI line with column densities of  $\log N(\text{OVI})\text{cm}^2 = (12.5 - 13, 13 - 14, > 14)$  (top panel) and O VII line of  $\log N(\text{OVI})\text{cm}^2 = (13 - 14, 14 - 15, > 15)$  (bottom panel). The blue dot-dashed curve in the top (bottom) panel shows the O VI (O VII) fraction as a function of gas temperature in the absence of photoionization.

comparable in numbers, consistent with Figure 14 below. Our results for O VI lines is broadly consistent with (Shull et al. 2011). Shull et al. (2011) find a bimodal distribution of O VI absorbers, one concentrating at  $(\delta, T)=(\sim 10, 10^{4.5}\text{K})$  and the other at  $(\delta, T)=(\sim 100, 10^{5.5}\text{K})$  (see their Figures 4,5).

Figure 8 shows the cumulative probability distribution functions as a function of absorber temperature for three subsets of O VI lines with column densities of  $\log N(\text{OVI})\text{cm}^2 = (12.5-13, 13-14, > 14)$  (top panel) and O VII line of  $\log N(\text{OVI})\text{cm}^2 = (13-14, 14-15, > 15)$  (bottom panel). We find that (39%, 43%, 61%) of O VI absorbers in the column density ranges of  $\log N(\text{OVI})\text{cm}^2 = (12.5 - 13, 13 - 14, > 14)$  have temperature greater than  $10^5\text{K}$ , (25%, 39%, 73%) of O VII absorbers in the column density ranges of  $\log N(\text{OVI})\text{cm}^2 = (13 - 14, 14 - 15, > 15)$  have temperature greater than  $10^5\text{K}$ . Our findings are in broad agreement with previous results obtained by our group (e.g., Cen et al. 2001; Cen & Ostriker 2006; Cen & Chisari 2011) and some other groups (e.g., Tepper-García et al. 2011; Shull et al. 2011), but in substantial disaccord with results of Oppenheimer & Davé (2009) and Oppenheimer et al. (2012) who find that photo-ionized O VI lines with temperature lower than  $10^5\text{K}$  make up the vast majority of O VI lines across the column density range  $\log N(\text{OVI})\text{cm}^2 = 12.5 - 15$ . Given the differences in simulation codes and in treatment of feedback processes, we cannot completely ascertain the exact cause for the different results. Nevertheless, the explanation given by Oppenheimer et al. (2012) that the lack of metal mixing in their SPH simulations plays an important role in contributing to the difference is further elaborated here.

Oppenheimer et al. (2012) find a large fraction of metal-carrying feedback SPH particles wound up in low density regions that have relatively high metallicity ( $\sim 1 Z_\odot$ ) and low temperature ( $T \sim 10^4\text{K}$ ). As a result, they find low-density, high-metallicity and low-temperature photo-ionized O VI absorbers to dominate the overall O VI absorber population in their SPH simulations. According to Tepper-García et al. (2011), they repeat simulations with the same feedback model used in Oppenheimer & Davé (2009) and Oppenheimer et al. (2012) but with metal heating included, and are unable to reproduce the dominance of low-temperature photoionized O VI absorbers seen in the latter. This leads them to conclude that lack of metal heating, in the presence of high-metallicity feedback SPH particles, is the cause of the dominance of low-density, high-metallicity and low-temperature photo-ionized O VI absorbers found in Oppenheimer & Davé (2009) and Oppenheimer et al. (2012). We suggest that this overcooling problem may have been exacerbated by lack of metal mixing. Consistent with this conjecture, while Tepper-García et al. (2011) suffer less severely from the metal overcooling problem (because of metal heating), the median metallicity of their O VI absorbers is still  $\sim 0.6 Z_\odot$ , substantially higher than that of our O VI absorbers,  $Z \sim 0.03 - 0.3 Z_\odot$ , even though their overall abundance of O VI absorbers is lower than observed by a factor of  $\sim 2$ . This noticeable difference in metallicity may be rooted in lack of metal mixing in theirs.

As we will show later (see Figure 13 below), the metallicity of simulated O VI in our simulations appears to better match observations. Despite that, it is desirable to directly probe the physical nature of O VI absorbers to test models by different simulation groups. One major difference between SPH simulations (e.g., Tepper-García et al. 2011; Oppenheimer et al. 2012) and AMR simulations (e.g., Smith et al. 2011, and this work) is that the former predict metallicity distributions that are peaked at  $(0.6-1) Z_{\odot}$  compared to peaks of  $\sim (0.05-0.2) Z_{\odot}$  in the latter. In addition, in the latter positive correlations between metallicity and O VI column density and between metallicity and temperature are expected, whereas in the former the opposite or little correlation seems to be true. Therefore, direct measurements of O VI metallicity and correlations between metallicity and other physical quantities would provide a good discriminator. Putting differences between SPH simulations of WHIM by different groups aside, what is in common among them is the dominance of low-density ( $\delta \leq 100$ ) O VI absorbers at all column densities. In the AMR simulations it is found that the collisionally ionized O VI absorbers, with density broadly peaked at  $\delta \sim 100$ , dominate (by 2 to 1) over photoionized O VI absorbers for  $N(\text{OVI}) \geq 10^{14} \text{cm}^{-2}$  population. Given these significant differences between SPH and AMR simulations, we suggest a new test, namely, the cross-correlation function between galaxies and strong [ $N(\text{OVI}) \geq 10^{14} \text{cm}^{-2}$ ] O VI absorbers. Available observations appear to point to strong correlations at relatively small scales  $\leq 300 - 700 \text{kpc}$  between luminous galaxies ( $\geq 0.1 L_*$ ) and  $N(\text{OVI}) \geq 10^{13.2-13.8} \text{cm}^{-2}$  O VI absorbers at  $z = 0 - 0.5$  (e.g., Stocke et al. 2006; Chen & Mulchaey 2009; Prochaska et al. 2011). We expect AMR simulated O VI absorbers to show stronger small-scale cross-correlations with galaxies than SPH simulated O VI absorbers thanks to the predicted dominance of O VI absorbers in low density (but higher metallicity) regions in the latter that are at larger distances from galaxies. When an adequate observational sample of Ne VIII absorbers becomes available, galaxy-Ne VIII may provide a still more sensitive test between photoionization models suggested by some SPH simulations and AMR simulations, because the N VIII line needs a still higher temperature to collisionally ionize and hence the contrast is still higher between the simulations. However, the shorter wavelengths of the Ne VIII lines at  $770\text{\AA}$  and  $780\text{\AA}$  require galaxies at  $z > 0.47$  to shift into the HST (COS or STIS) observable band, for which current galaxy surveys will only be able to probe most luminous galaxies ( $L > L_*$ ). Detailed calculations and comparisons to observations will be needed to ascertain these expectations to nail down their physical nature and to constrain feedback models.

The rapid rise in the cumulative fraction in the temperature range  $\log T = 5.5 \pm 0.1$  in the top panel of Figure 8 reflects the concentration of collisionally ionized O VI lines in that temperature range, supported the blue dot-dashed curve showing the collisional ionization fraction of O VI as a function of temperature. This feature is most prominent in the high column density O VI population with  $\log N(\text{OVI}) \text{cm}^2 > 14$  (green dashed curve), simply stating the fact that collisional ionization is dominant in high column density O VI lines.

For O VII there is a similar feature except that it is substantially broader at  $\log T = 6.0 \pm 0.4$ , which is consistent with the ionization fraction of O VII as a function of temperature in the collisional ionization dominated regime, shown as the blue dot-dashed curve in the bottom panel of Figure 8. For O VI lines with column density in the range  $\log N(\text{OVI})\text{cm}^2 = 12.5 - 14$  we see a relative dearth of absorbers in the temperature range  $\log T = 4.8 - 5.4$ , a regime where neither collisional ionization nor photoionization is effective due to structured multi-phase medium (i.e., positive correlation between density and temperature in this regime, see Figure 17 below); at still lower temperature  $\log T < 4.8$  (and low density due to the positive correlation), the curve displays a rapid ascent due to its entry into the photoionization dominated regime. Analogous behaviors and explanations can be said for O VII absorbers.

We see earlier in Figure 6 that  $b$  is not a good indicator of the temperature of absorbing gas. It is thus useful to quantify the fraction of absorbers at a given  $b$  whose temperature is in the WHIM regime. Figure 9 shows the fraction of O VI (top panel) and O VII (bottom panel) absorbers that is in WHIM temperature range of  $10^5 - 10^7\text{K}$  as a function of  $b$ . Broadly speaking, above the threshold (thermally broadened Doppler width of  $10.16\text{km/s}$  for a gas at temperature of  $10^5\text{K}$ ), the WHIM fraction is dominant at  $\geq 50\%$  for both O VI and O VII lines, but only close to  $100\%$  when  $b$  is well in excess of  $100\text{km/s}$ . This again indicates the origin of the O VI absorbing gas whose random motions are far from completely thermalized, consistent with its (mostly) intergalactic nature. The approximate fitting curve (blue curve) for the column density weighted histogram for O VI shown in Figure 9 can be formulated as the following equation:

$$\begin{aligned} f(\text{OVI}) &= 0.20 & \text{for } b < 10 \text{ km/s} \\ &= 0.0026(b - 10) + 0.6 & \text{for } b = 10 - 160 \text{ km/s} \\ &= 1 & \text{for } b > 160 \text{ km/s} \end{aligned} \tag{2}$$

As already indicated in Figure 4 that a substantial fraction of broad but shallow absorbers may be missing in current observational data, here we quantify it further. Figure 10 shows four cumulative probability distribution functions as a function of  $b$  for four subsets of O VI (top panel) and O VII (bottom panel) lines of differing column densities. To give some quantitative numbers, (15%, 20%, 26%, 39%) of O VI absorbers with  $\log N(\text{O VI}) = (12.5 - 13, 13 - 13.5, 13.5 - 14, > 14)$  have  $b > 40 \text{ km/s}$ ; the fractions drop to (1%, 2%, 4%, 7%) for  $b > 80 \text{ km/s}$ . Similarly, (17%, 46%, 77%, 88%) of O VII absorbers with  $\log N(\text{O VI}) = (13 - 14, 14 - 15, 15 - 16, > 16)$  have  $b > 40 \text{ km/s}$ , with (2%, 9%, 29%, 30%) having  $b > 80 \text{ km/s}$ . With COS observations of substantially higher sensitivities, broad O VI lines are begun to be detected (Savage et al. 2010). A direct, statistical comparison between simulation

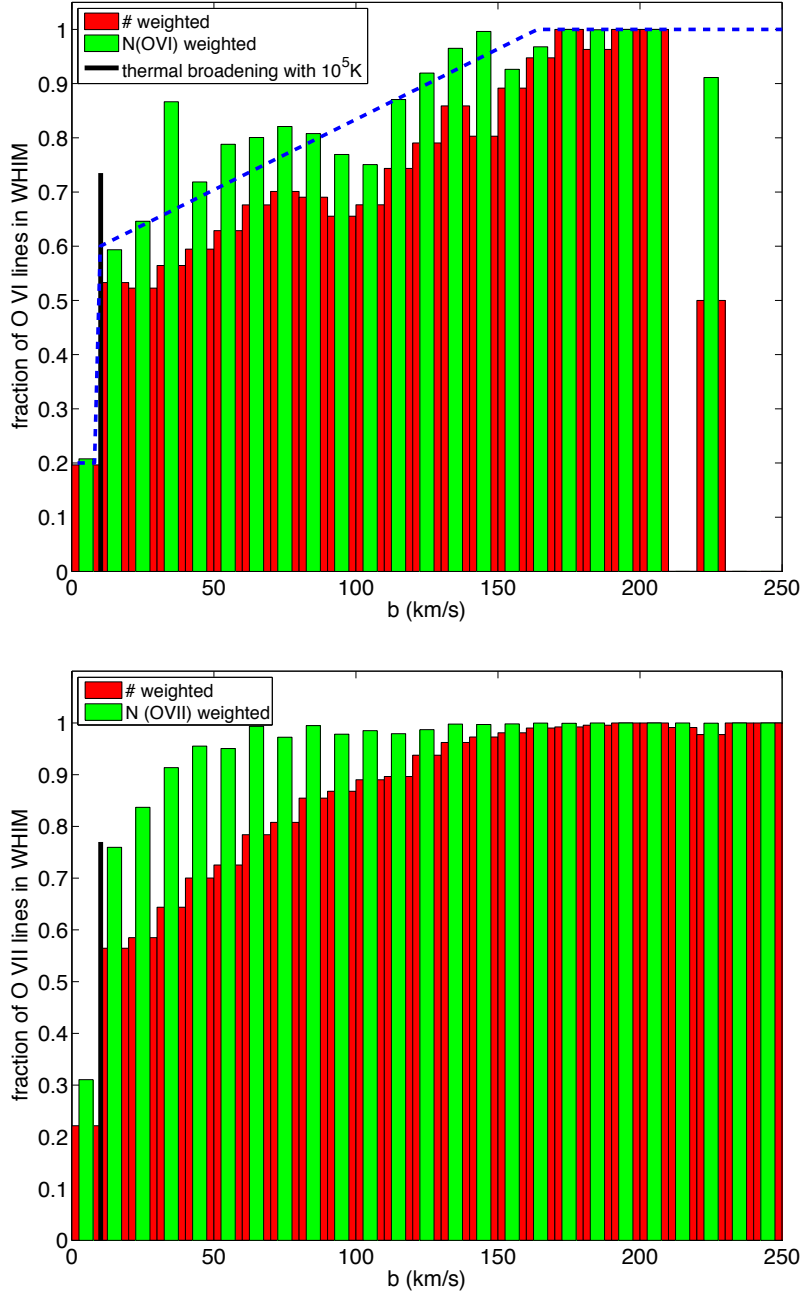


Fig. 9.— shows the fraction of O VI (top panel) and O VII (bottom panel) absorbers that is in WHIM temperature range of  $10^5 - 10^7$  K as a function of  $b$ . The red and green histograms are number and column density weighted, respectively, including only lines with column density above  $10^{13}\text{cm}^{-2}$  in the case of O VI and  $10^{14}\text{cm}^{-2}$  for O VII. The vertical black line indicates  $b$  for a purely thermally broadened line at a temperature of  $10^5$  K. The approximate fitting curve indicated by blue dashed line is given in Equation (2).

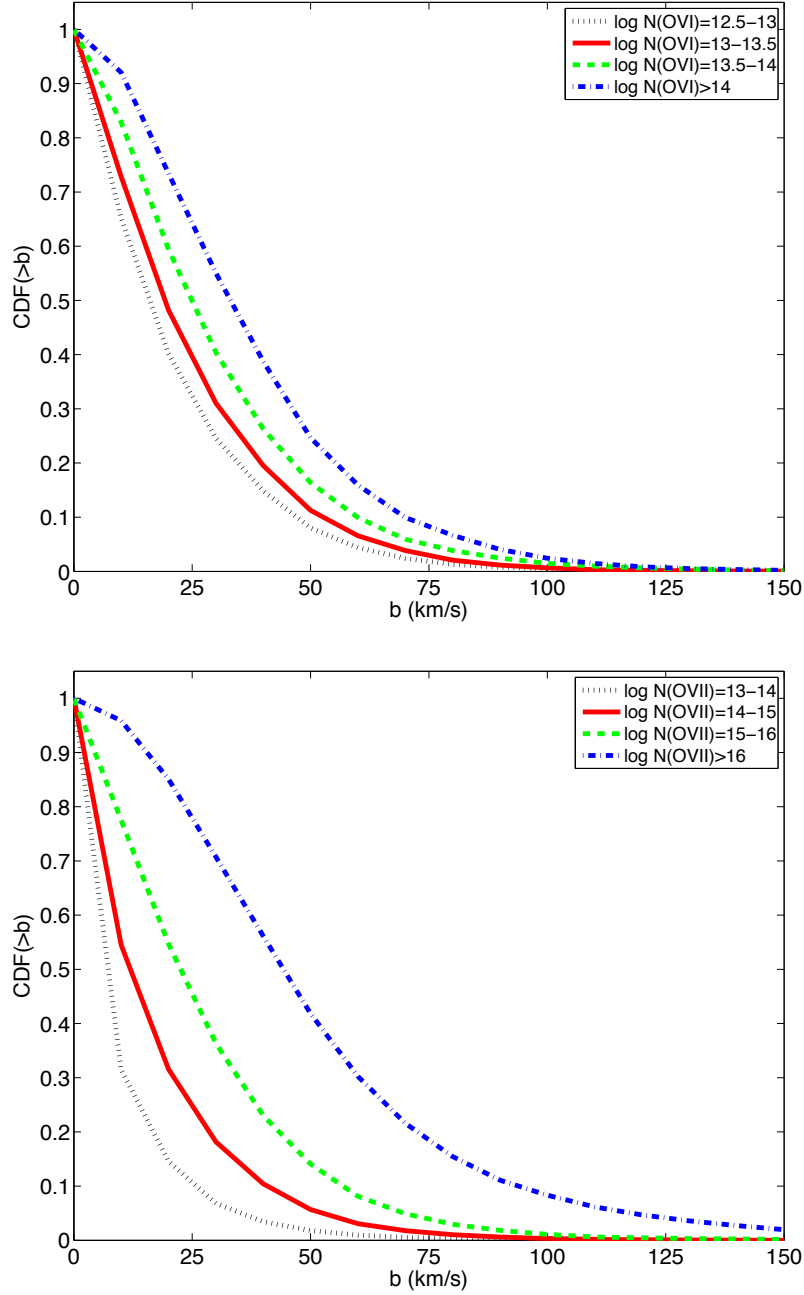


Fig. 10.— Top panel shows four cumulative probability distribution functions as a function of  $b$  for four subsets of O VI lines in the four column density ranges:  $\log N(\text{OVI})\text{cm}^2 = 12.5-13$  (black dotted curve),  $\log N(\text{OVI})\text{cm}^2 = 13-13.5$  (red solid curve),  $\log N(\text{OVI})\text{cm}^2 = 13.5-14$  (green dashed curve) and  $\log N(\text{OVI})\text{cm}^2 > 14$  (blue dot-dashed curve). Bottom panel shows four cumulative probability distribution functions as a function of  $b$  for four subsets of O VII lines in the four column density ranges:  $\log N(\text{OVI})\text{cm}^2 = 13-14$  (black dotted curve),  $\log N(\text{OVI})\text{cm}^2 = 14-15$  (red solid curve),  $\log N(\text{OVI})\text{cm}^2 = 15-16$  (green dashed curve) and  $\log N(\text{OVI})\text{cm}^2 > 16$  (blue dot-dashed curve).

results found here and observations will be possible in the near future. It will be extremely interesting to see if there is indeed a large population of broad but shallow O VI lines still missing. That is also important, because, if that is verified, one will have more confidence on the results for O VII lines, which suggest that the O VII lines may be substantially broader than a typical thermally broadened width of 40 – 50 km/s. Additional useful information is properties of other lines, including Ly $\alpha$ , which we will present in a subsequent paper. Since the expected  $b$  of O VII lines is still substantially smaller than spectral resolution of Chandra and XMM-Newton X-ray instruments, it does not make much difference for extant observations. However, it should be taken into consideration in designing future X-ray telescopes to probe WHIM in absorption or emission (e.g., Yao et al. 2012).

Figure 11 shows absorbers in the metallicity-overdensity plane. The apparent anti-correlation between metallicity and overdensity with a log slope of approximately  $-1$  for the mostly collisional ionization dominated population (red circles) is simply due to the fact that the absorbers near the chosen column density cutoff dominate the numbers and that collisional ionization rate is density independent. Similarly, the apparent anti-correlation between metallicity and overdensity with a log slope of approximately  $-2$  for the mostly photoionization dominated population (blue squares) is due to the fact that photo-ionization fraction is proportional to density. So one should not be misled to believe that there is an anti-correlation between gas metallicity and overdensity in general; the opposite is in fact true (see Figure 18 below). In Figure 12 we project two subsets of absorbers onto the metallicity- $b$  plane. Because of complex behaviors seen in Figure 11 and the additional role played by complex temperature and velocity distributions, one may not be surprised to see the large dispersions in metallicity at a given  $b$ . The metallicity distribution is seen to be, to zero-order within the large dispersions, nearly independent of  $b$ . When metallicity of O VI and O VII absorbers can be measured directly in the future, this prediction may be tested. No further detailed information on this shall be given here due to its still more futuristic nature in terms of observability, except noting that the weak trends can be understood and these trends are dependent upon the column density cuts.

Figure 13 shows the mean metallicity as a function of column density for O VI (red circles) and O VII absorbers (blue squares). We see that a substantial dispersion of about 0.5-1 dex is present for all column density bins. The mean metallicity for O VI lines increases by 0.9 dex from  $[Z/H] \sim -1.3$  at  $N(\text{OVI}) = 10^{13}\text{cm}^{-2}$  to  $[Z/H] \sim -0.4$  at  $N(\text{OVI}) = 10^{15}\text{cm}^{-2}$ . For O VII lines the mean metallicity increases by 0.4 dex from  $[Z/H] \sim -1.1$  at  $10^{14}\text{cm}^{-2}$  to  $[Z/H] \sim -0.7$  at  $10^{16}\text{cm}^{-2}$ . The trend of increasing metallicity with increasing column density is consistent with the overall trend that higher density regions, on average, have higher metallicity, at least in the density range of interest here (see Figure 11 below). It is noted that the mean metallicity for O VII absorbers is, on average, lower than that for O VI lines at a fixed column density for the respective ions. This and some other relative behaviors between O VI and O VII seen in Figure 13 merely reflect the facts (1) that the



product of oscillator strength and restframe wavelength of O VII line is about a factor of 10 lower than that of O VI, (2) the peak collisional ionization fraction for O VII is about a factor of 5 higher than that of O VI, and (3) the peak width for collisional ionization temperature for O VII is larger by a factor of  $\sim 3$  than that of O VI (see Figure 8). Examination of the C+P (collisional + photoionization) model with distributed feedback (which is closest to our feedback model) in Figure 17 of Smith et al. (2011) reveals that the average metallicity increases from  $\sim -1.0$  to  $\sim 0.0$  for  $N_{\text{OVI}}$  from  $10^{12}\text{cm}^{-2}$  to  $10^{15}\text{cm}^{-2}$ , which should be compared to an increase of metallicity from  $\sim -1.5$  to  $\sim -0.5$ . Thus, our results are in good agreement with Smith et al. (2011) except that their metallicity is uniformly higher by a factor of  $\sim 3$ .

While there are substantial disagreements among the SPH and AMR simulations with respect to the metallicity of O VI absorbers, it is fair to say that a median value of  $0.1 - 1 Z_{\odot}$  encompasses them. Given that, some quantitative physical considerations are useful here. The cooling time for gas of  $\delta = 100$ ,  $T = 10^{5.5}\text{K}$  and  $Z = 0.1 Z_{\odot}$  at  $z = 0$  is  $\sim 0.05 t_H$  ( $t_H$  is the Hubble time at  $z = 0$ ) (this already takes into account metal heating by the X-ray background; it should be noted that the X-ray background at  $z \sim 0$  is still quite uncertain (e.g., Shull et al. 2011)). This indicates that the O VI-bearing gas of  $T \sim 10^{5.5}\text{K}$  and  $\delta \geq 100$ , in the absence of other balancing heating processes, can only spend a small fraction of a Hubble time at the temperature for optimal O VI production via collisional ionization. This has two implications. First, O VI absorbers at  $\delta \geq 100 \times (Z/0.1 Z_{\odot})^{-1}$  is transient in nature and their appearance requires either constant heating of colder gas or higher temperature gas cooling through. Which process is more responsible for O VI production will be investigated in a future study. Second, the metal cooling that is linearly proportional to gas metallicity may give rise to an interesting “selection effect”, where high metallicity O VI gas in dense regions, having shorter cooling time than lower metallicity O VI gas of the same density, would preferentially remove itself from being O VI productive by cooling, leaving behind only lower metallicity gas at O VI-bearing temperatures. We suggest that this selection effect may have contributed to a much reduced proportion of collisionally ionized O VI lines in SPH simulations that lack adequate metal mixing; in other words, dense metal “bullets” of SPH particles either cools very quickly to  $\sim 10^4\text{K}$  or they have reached regions of sufficiently low density before that happens. The results of Oppenheimer et al. (2012) appear to suggest, in the context of this scenario, that the feedback metal-bearing SPH particles have cooled to  $\sim 10^4\text{K}$ , before they can reach low density regions to avoid severe cooling, thus resulting in high-metallicity, low-density, photoionized O VI lines when they eventually wind up in low density regions. An analogous situation occurs in Tepper-García et al. (2011) SPH simulations but with two significant differences from those of Oppenheimer et al. (2012): (1) in the former the inclusion of metal heating (due to photoionization of metal species) keeps the corresponding SPH particles at a higher temperature floor ( $\sim 10^{4.5-5}\text{K}$  barring adiabatic cooling) than in the latter, and (2) “smoothed” metallicity used in the former to compute

metal cooling/heating rates has reduced the metal cooling effects (which still dominate over metal heating at  $T \geq 10^5\text{K}$ ) compared to the case without such smoothing in the latter.

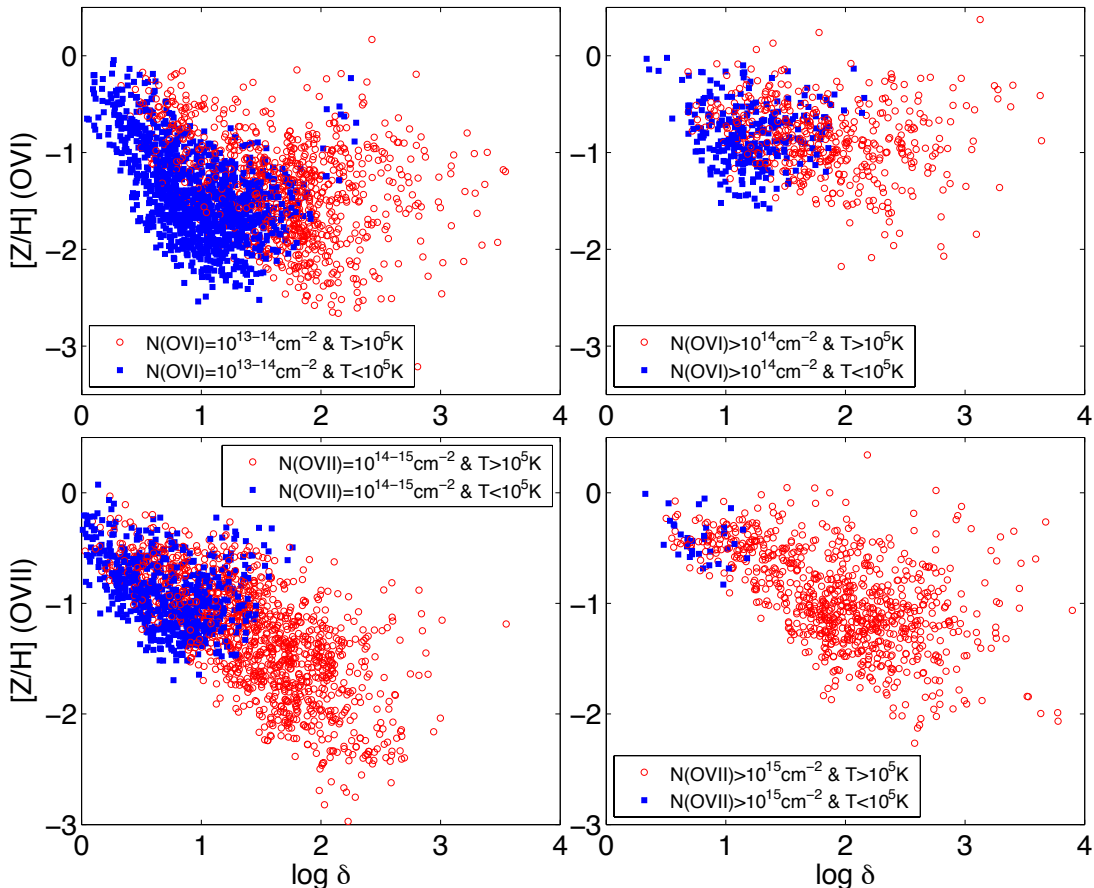


Fig. 11.— shows absorbers in the metallicity-overdensity plane for O VI line with  $N(\text{OVI}) = 10^{13-14}\text{cm}^{-2}$  (top left panel) and  $N(\text{OVI}) > 10^{14}\text{cm}^{-2}$  (top right panel). The bottom two panels show O VII line with  $N(\text{OVI}) = 10^{14-15}\text{cm}^{-2}$  (bottom left panel) and  $N(\text{OVI}) > 10^{15}\text{cm}^{-2}$  (bottom right panel). Within each panel, we have broken up the absorbers into two subsets using temperature:  $T > 10^5\text{K}$  (red circles) and  $T < 10^5\text{K}$  (blue squares).

### 3.3. Coincidence Between O VI and O VII Lines

In §3.1 we show that some of the primary observable properties of simulated O VI lines, including line incidence rate, are in excellent agreement with observations. In §3.2 we have shown various physical properties underlying the observables of both lines. Before presenting quantitative coincidence rates between O VI and O VII lines, it is useful to further check

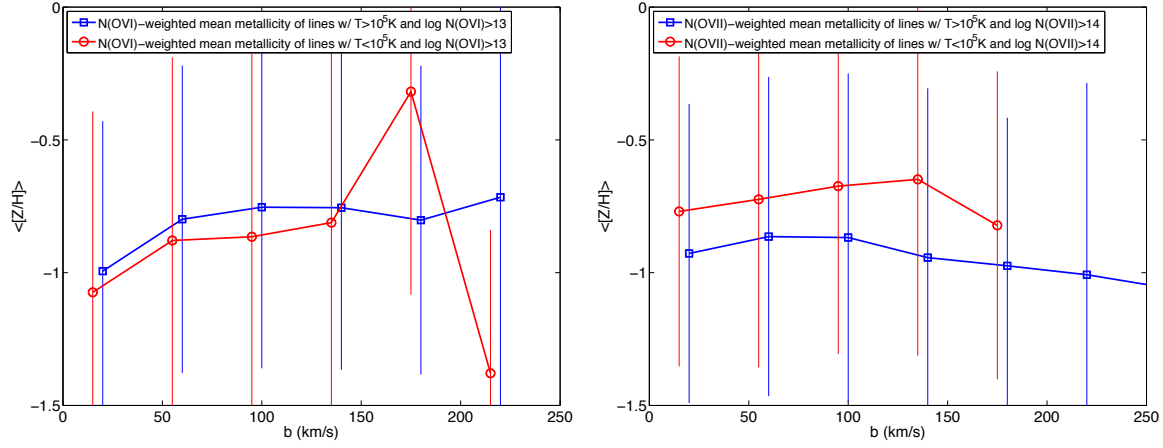


Fig. 12.— shows the mean absorber metallicity as a function of  $b$  for O VI line with column density above  $10^{13}\text{cm}^{-2}$  (top panel) and O VII line with column density above  $10^{14}\text{cm}^{-2}$  (bottom panel). Within each panel, we have broken up the absorbers into two subsets using temperature:  $T > 10^5\text{K}$  (blue squares) and  $T < 10^5\text{K}$  (red circles).

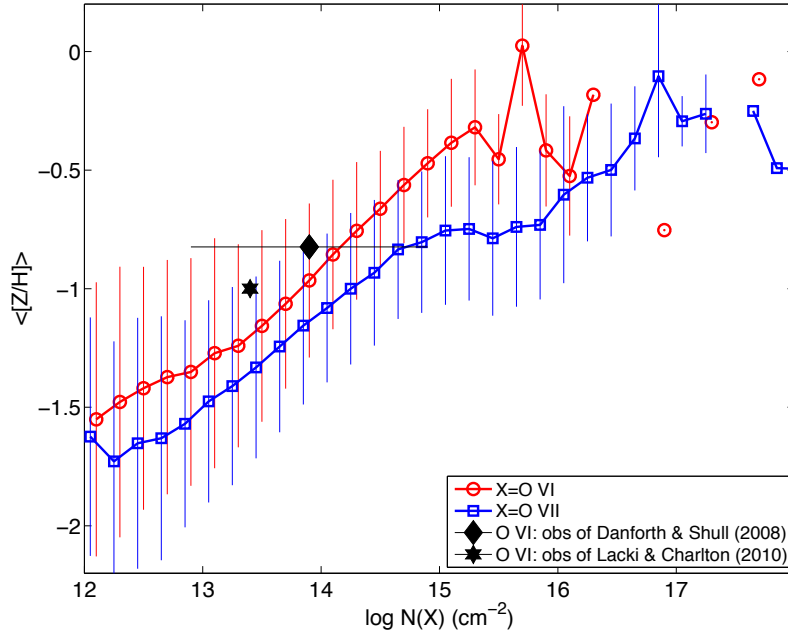


Fig. 13.— shows the mean metallicity as a function of column density for O VI (red open circles) and O VII (blue open squares) lines. Also shown as solid symbols are observational data. It is likely that the observational errorbars are underestimated.

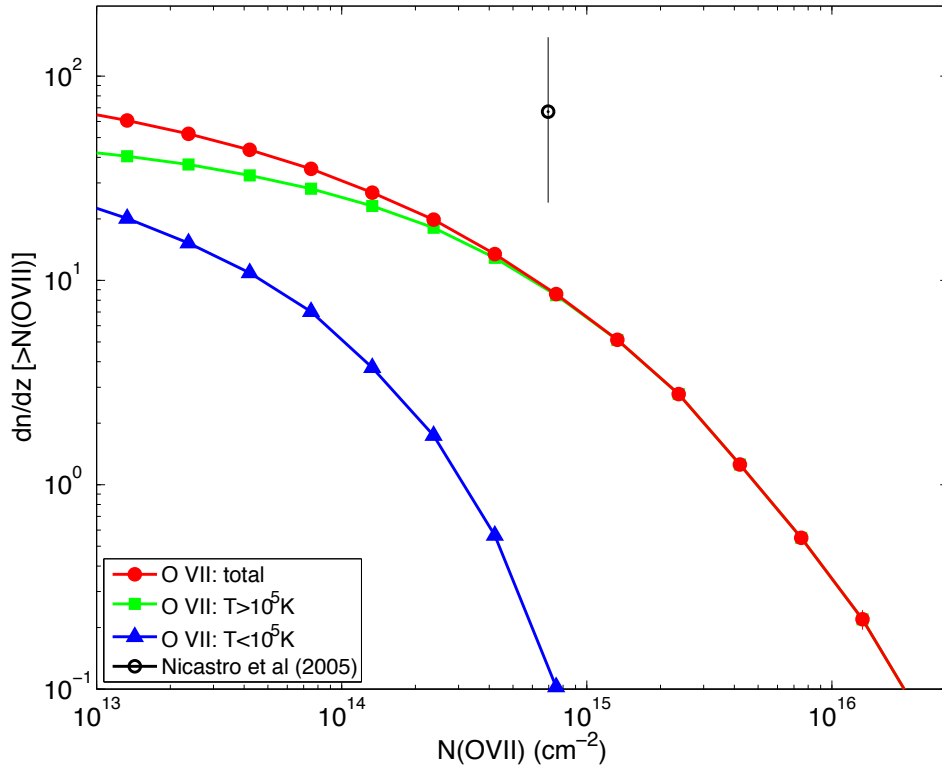


Fig. 14.— shows the cumulative O VII line density as a function of column density, defined to be the number of lines per unit redshift at the column density greater than the value at the x-axis. The red solid dots, green squares and blue triangles are the total, collisionally ionized and photo-ionized lines, respectively. Also shown as a black open circle is the observation of Nicastro et al. (2005a) with  $1\sigma$  errorbar. Note that the quantify shown in the y-axis of Figure 5 is differential, not cumulative density.

the O VII line incidence rate to assess the self-consistency of our simulations with extant observations. Figure 14 shows the cumulative O VII line density as a function of column density. We also show the implied observed line density, under the assumption that the detection reported by Nicastro et al. (2005a) is true. We see that the claimed observational detection is about  $2\sigma$  above or a factor of  $\sim 7$  higher than our predicted central value at the column density  $\geq 7 \times 10^{14} \text{ cm}^{-2}$ . Our model is clearly in a more comfortable situation, if the claimed observational detection turns out to be negative. As discussed in the introduction the detection reported by Nicastro et al. (2005a) is presently controversial. This highlights the urgent need of higher sensitivity X-ray observations of this or other viable targets that could potentially place strong constraints on the model.

We now turn to the coincidences between O VI and O VII lines. The top panel of

Figure 15 shows the cumulative probability distribution functions as a function of velocity displacement of having a coincidental O VII line above the indicated equivalent width for an O VI line of a given equivalent width. We see that O VI lines of equivalent width in the range 50 – 200mÅ have (38%, 31%, 10%) probability of finding an O VII line with equivalent width greater than (0.1, 0.5, 2)mÅ within a velocity displacement of 150 km/s. The vast majority of coincidental O VII lines for O VI lines for those equivalent widths in question are concentrated within a velocity displacement of  $\leq 50$  km/s and more than 50% at  $\leq 25$  km/s.

The bottom panel of Figure 15 shows the cumulative probability distribution functions as a function of velocity displacement of having a coincidental O VI line above the indicated equivalent width for an O VII line of a given equivalent width. It is seen that for O VII lines of equivalent width in the range 2 – 4mÅ have a 17 – 27% probability of finding an O VI line with equivalent width in the range 5 – 100mÅ within a velocity displacement of 150 km/s. Likewise, the vast majority of coincidental O VI lines for O VII lines for those equivalent widths in question are concentrated within a velocity displacement of  $\leq 50$  km/s and more than 80% at  $\leq 25$  km/s.

The results shown in Figure 15 presently can not be compared to observations, because there is no definitive detection of O VII absorbers, although there are many detected O VI absorbers. Thus, we use the stacking method of Yao et al. (2009) to enable a direct comparison with available observations. The top panel of Figure 16 shows the expected mean O VII column density at the location of detected O VI lines of column density indicated by the x-axis, compared to the  $3\sigma$  upper limits from observations of Yao et al. (2009) shown as black triangles. We see that the non-detection of O VII lines, or more precisely, a  $3\sigma$  upper limit on the mean column of O VII lines for detected O VI lines of column density in the range  $\log N(\text{OVI})\text{cm}^2 = 13.6 - 14.1$ , is fully consistent with our simulations. The reported  $3\sigma$  upper limit is above the expected value by a factor of 2.5 – 4. This suggests that a factor of  $\sim 10$  increase in sample size or sensitivity will be able to yield a definitive detection of O VII column density using the stacking technique even without detection of individual O VII absorbers. The bottom panel of Figure 16 shows the expected mean O VI column density at the location of detected O VII lines of column density indicated by the x-axis.

It is evident from Figures 15,16 that O VI and O VII lines are coincidental only in a limited sense. We attribute the limited coincidence of O VII lines for O VI lines primarily to two situations for O VI producing regions. A line of sight that intersects an O VI producing region does not necessarily intersect a strong O VII producing region along the same line of sight, either because the temperature of the overall region does not reach a high enough value to be strong O VII bearing, or because the intersected O VI region is laterally an outskirts of an onion-like structure where the more central, higher temperature, O VII region makes up a smaller cross section. The former case should be ubiquitous, because weaker gravitational

shocks that produce regions of temperature, say,  $10^{5.5}\text{K}$  are more volume filling than stronger gravitational shocks giving rise to regions of temperature, say,  $10^{6.0}\text{K}$ . In addition, feedback shocks from star formation tend to be weaker than required to collisionally produce O VII at the spatial scales of interest here. In other words, one expects to see many O VI-bearing regions that have no associated O VII-bearing sub-regions. The latter case where hotter but smaller regions are surrounded by cooler regions is expected to arise naturally around large virialized systems such as groups and clusters of galaxies. A more quantitative but still intuitive physical check of the obtained results is not straight-forward, without performing a much more detailed study of individual physical regions that produce O VI and O VII absorbers. We shall reserve such a study for the future.

The situation of coincidental O VI lines for given O VII lines might appear to be less ambiguous at first sight in the sense that the hotter central, O VII-producing regions should be surrounded by cooler regions and thus one might expect that the line of sight that intersects a strongly O VII-producing region should automatically intersect cooler regions that would show up as O VI absorbers. While it is true that a hot region is in general surrounded by cooler regions, it is not necessarily true that a hot  $10^6\text{K}$ , O VII-bearing gas is surrounded by significant  $10^{5.5}\text{K}$ , O VI-bearing gas. For example, one may have a post-shock region of temperature  $10^6\text{K}$  that is surrounded only by pre-shocked gas that is much colder than  $10^{5.5}\text{K}$ . We note that for a gas of  $\delta = 100$ ,  $T = 10^6\text{K}$  and  $Z = 0.3 Z_\odot$  at  $z = 0$ , its cooling time is  $t_{cool} \sim 0.5t_H$  ( $t_H$  is the Hubble time at  $z = 0$ ). This means that O VII-bearing WHIM gas at  $\delta \leq 100$ , which has been heated up by shocks to  $T \geq 10^6\text{K}$ , is unlikely to cool to  $T \sim 10^{5.5}\text{K}$  to become O VI rich gas. On the other hand, the cooling time for gas of  $\delta = 100$ ,  $T = 10^{5.5}\text{K}$  and  $Z = 0.1 Z_\odot$  at  $z = 0$  is  $\sim 0.05t_H$ , as noted earlier. Thus, it is physically possible that sharp interfaces between hot ( $T \geq 10^6\text{K}$ ) and cold  $T \leq 10^5\text{K}$  gas develop. The simulations do not include thermal conduction, which can be shown to be unimportant here. The electron mean free path (mfp) is  $0.44(T/10^6\text{K})^2(\delta/100)^{-1}\text{kpc}$ , adopting the standard Spitzer value. The likely presence of magnetic fields (not treated here) would further reduce the mfp by an order of magnitude (e.g., Cowie & McKee 1977). Thus, thermal conduction is insignificant and multi-phase media is expected to exist.

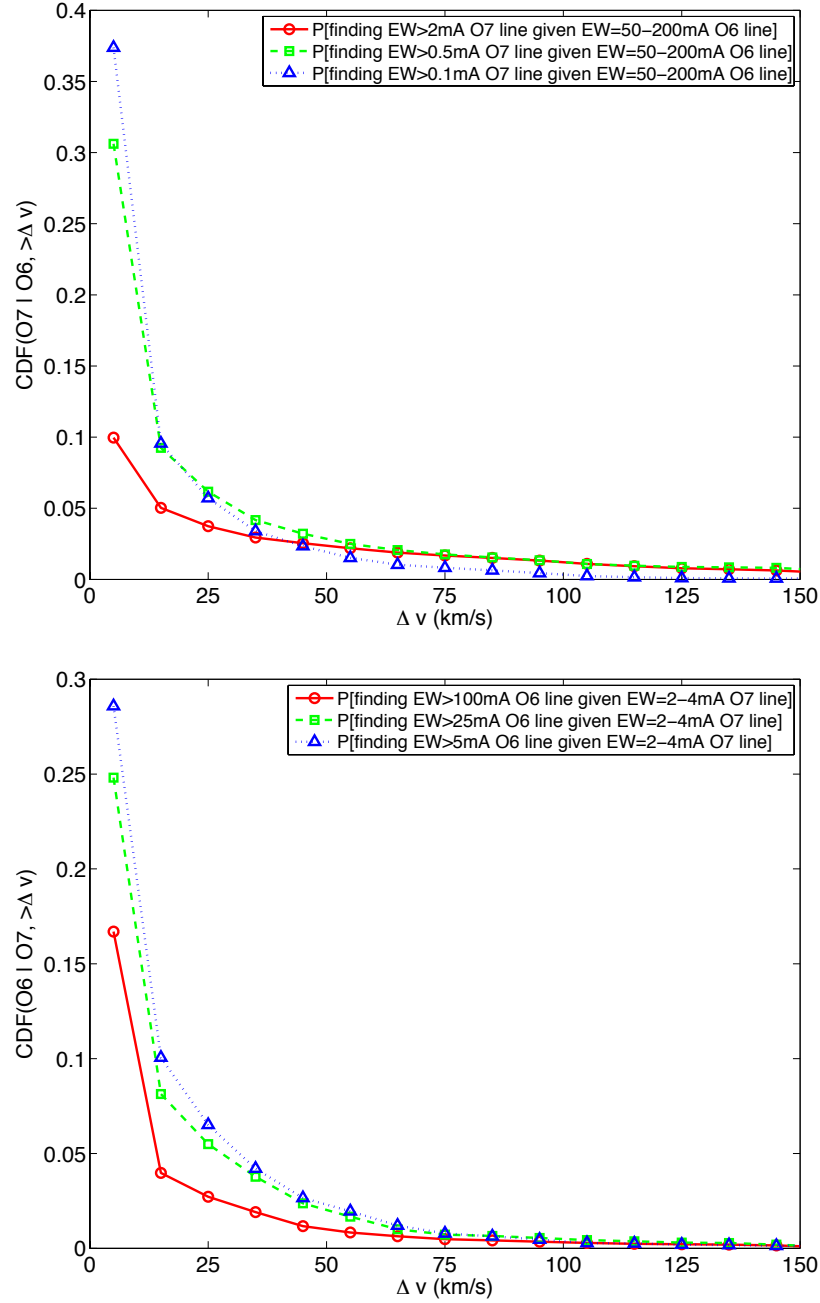


Fig. 15.— Top panel shows the cumulative probability distribution functions as a function of velocity displacement of having a coincidental O VII line above the indicated equivalent width for an O VI line of a given equivalent width. Bottom panel shows the cumulative probability distribution functions as a function of velocity displacement of having a coincidental O VI line above the indicated equivalent width for an O VII line of a given equivalent width.

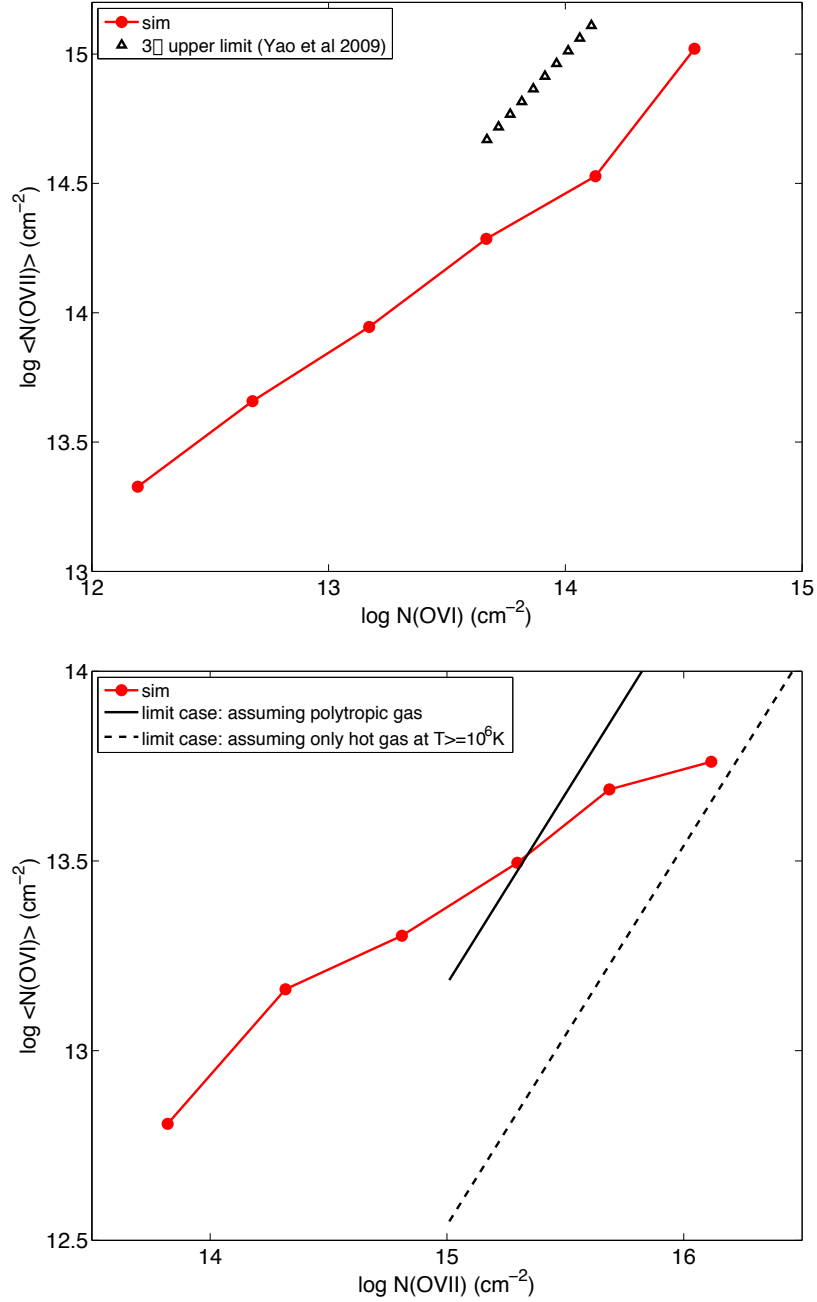


Fig. 16.— The top panel shows the expected mean O VII column density at the location of detected O VI lines of column density indicated by the x-axis. Also shown as black triangles are  $3\sigma$  upper limits from observations of Yao et al. (2009). The bottom panel shows the expected mean O VI column density at the location of detected O VII lines of column density indicated by the x-axis. The solid and dashed straight lines are possible limit cases based on simple physical considerations.



Equipped with this information and adopting the simpler implied geometry allows for a simple physical check of the results in the bottom panel of Figure 16, as follows. We will take two separate approaches to estimate this. The first approach assumes a polytropic gas in the temperature range relevant for O VI and O VII collisional ionization. In the top panel of Figure 17 we show the entire temperature-overdensity phase diagram for the refined region in the C run. Note that the gas density reaches about 1 billion times the mean gas density, corresponding to  $\sim 100\text{cm}^{-3}$ , i.e., star formation regions. For the regions of present relevance, the density range is about 10 – 300 times the mean density, illustrated by the upper part of the red tornado-like region near the middle of the plot. It is useful to note that for this density range, the gas mass is dominated by gas in the temperature range of  $10^5 - 10^7\text{K}$ , i.e., WHIM. Because of this reason, it is a valid exercise to compute the mean pressure as a function of overdensity, at least for the density range relevant for WHIM, shown in the bottom panel of Figure 17. We see that for the WHIM overdensity range of 10 – 300, the adiabatic index  $5/3$ , shown as the dashed line, provides an excellent approximation for the polytropic index of the gas. It is also necessary to have a relation between gas metallicity as a function of gas overdensity, shown in Figure 18. We only note that the metallicity is generally an increasing function with density above one tenth of the mean density, that the sharp rise of metallicity below one tenth of the mean density is due to metal-enrich galactic winds escaping into the low density regions, and that for our present purpose concerning the WHIM overdensity range of 10 – 300 the metallicity roughly goes as  $Z \propto \delta^{0.4}$ , as indicated by the dashed line.

Given the information in Figures 17, 18 we can now proceed to estimate the expected O VI column at a given O VII column density, i.e.,  $\langle N(\text{OVI}) \rangle / \langle N(\text{OVII}) \rangle$ , assuming both are dominated by collisional ionization. The O VI column density may be roughly approximated as  $\langle N(\text{OVI}) \rangle \propto f(\text{OVI}) \Delta \log T(\text{OVI}) \rho(\text{OVI}) Z(\text{OVI}) L(\text{OVI})$ , where  $f(\text{OVI}) = 0.22$  at  $\log T(\text{OVI})/\text{K} = 5.5$ ,  $\Delta \log T(\text{OVI}) = 0.2$ ,  $\rho(\text{OVI})$ ,  $Z(\text{OVI})$  and  $L(\text{OVI})$  are the peak collisional ionization fraction for O VI, the FWHM of the logarithmic temperature of the collisional ionization peak (see the blue curve in the top panel of Figures 8), the density of the O VI absorbing gas, the metallicity of the O VI absorbing gas and the physical thickness of the O VI absorbing gas, respectively. We have an exactly analagous relation for O VII, with  $f(\text{OVII}) = 1$ ,  $\log T(\text{OVII}) = 6$ ,  $\Delta \log T(\text{OVII}) = 0.7$ . With an additional assumption that the characteristic thickness at a given density goes as  $L(\text{OVI}) \propto \rho(\text{OVI})^{1/3}$  (i.e., mass distribution across log density is roughly uniform), we can now evaluate the column density ratio

$$\begin{aligned} \frac{\langle N(\text{OVI}) \rangle}{\langle N(\text{OVII}) \rangle} &= \frac{f(\text{OVI})}{f(\text{OVII})} \frac{\Delta \log T(\text{OVI})}{\Delta \log T(\text{OVII})} \frac{\rho(\text{OVI})}{\rho(\text{OVII})} \frac{Z(\text{OVI})}{Z(\text{OVII})} \frac{L(\text{OVI})}{L(\text{OVII})} \\ &= \frac{f(\text{OVI})}{f(\text{OVII})} \frac{\Delta \log T(\text{OVI})}{\Delta \log T(\text{OVII})} \left( \frac{T(\text{OVI})}{T(\text{OVII})} \right)^{(2/3+\alpha)/(\gamma-1)} = 0.015, \end{aligned} \quad (3)$$

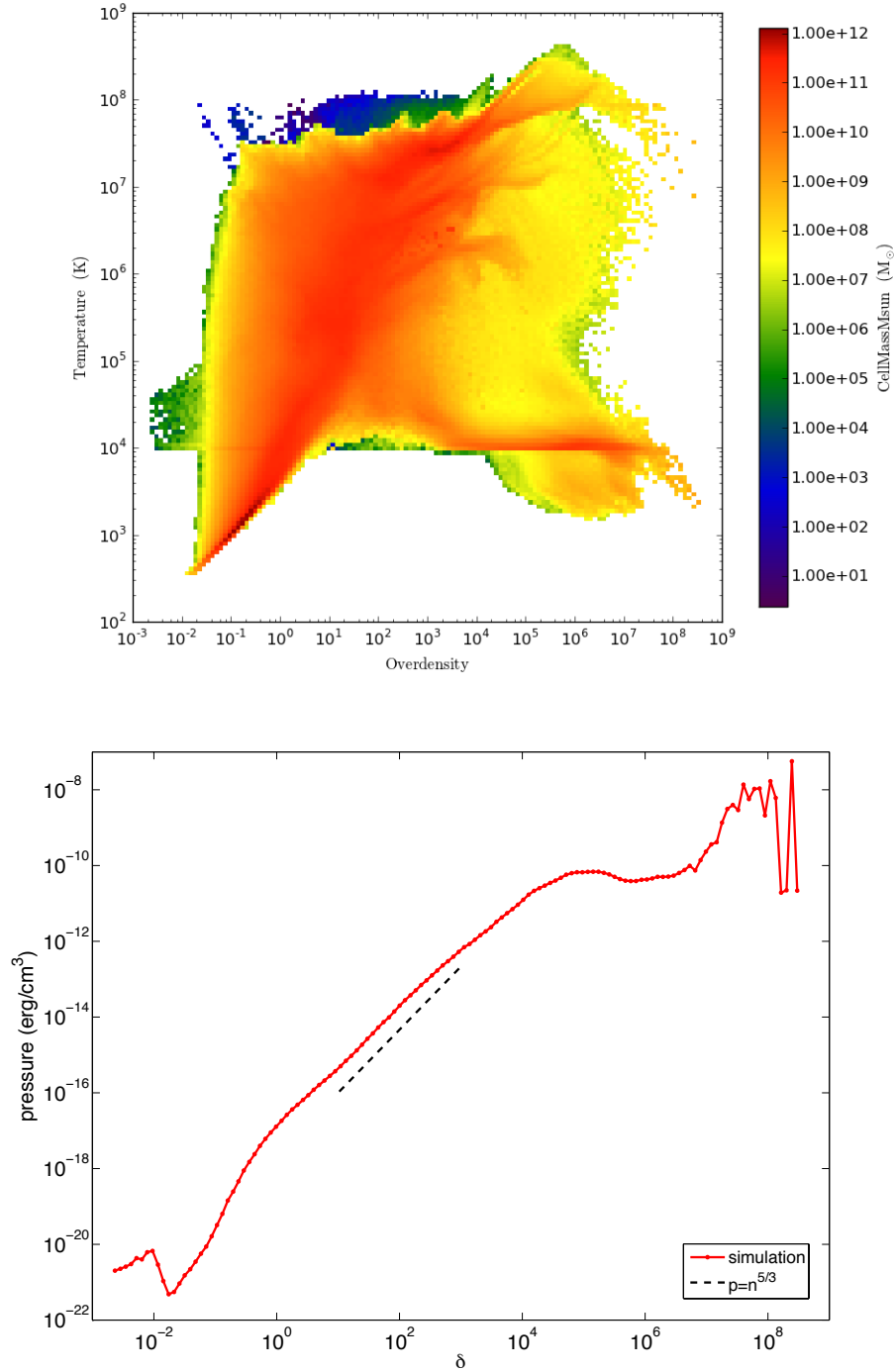


Fig. 17.— Top panel shows mass weighted phase diagram in the temperature-overdensity plane for the refined region in the C run. The bottom panel shows the mean pressure as a function of overdensity averaged over all cells in the regions in the C run. The black dashed line indicates the slope for polytropic gas of index  $5/3$  (i.e., the adiabatic index), which provides a good approximation to the simulation in the overdensity range  $10 - 300$  that is most pertinent to the absorbing WHIM in O VI and O VII.

where  $\alpha = 0.4$  and  $\gamma = 5/3$  are used, as indicated in Figures 18 and Figures 17, respectively. This resulting ratio is shown as the solid line in the bottom panel of Figure 16, which we expect to an approximate upper limit of the true ratio, since it implies the presence of O VI-bearing gas for every O VII line.

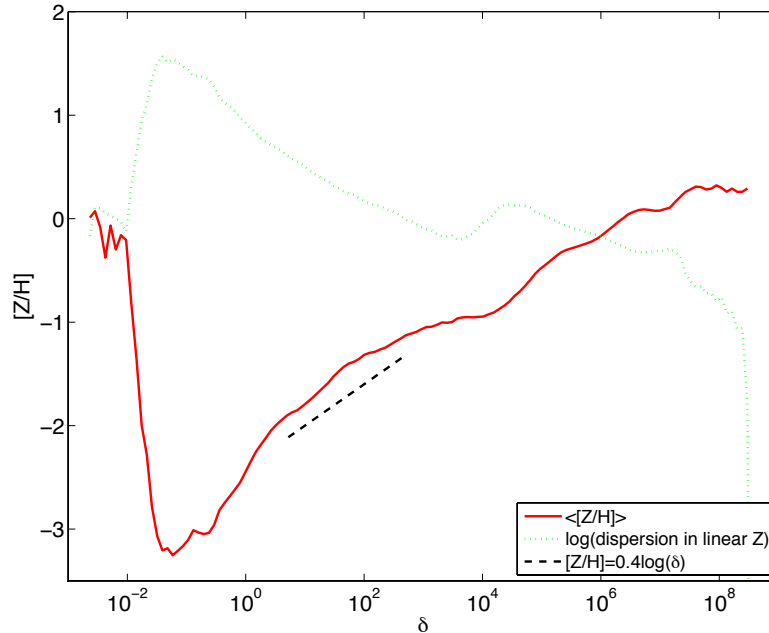


Fig. 18.— shows the mean gas metallicity (red solid curve) as a function of overdensity averaged over all cells in the refined region of the C run. Also shown as the green dotted curve is the logarithm of the dispersion in  $Z$  (linear metallicity). The black dashed line indicates the logarithmic slope of 0.4, which provides a good approximation to the simulation in the overdensity range 10 – 1000 relevant to absorbing WHIM in O VI and O VII.

Our second approach likely gives an approximate lower bound on  $\langle N(\text{OVI}) \rangle / \langle N(\text{OVII}) \rangle$ . We assume that the O VII-bearing gas is at the peak temperature of  $10^6 \text{ K}$  and is surrounded by gas that has a temperature that is much lower than  $10^{5.5} \text{ K}$  (neglecting photoionization for the moment), in which case the coincidental O VI line is produced by the same temperature gas that produces the O VII line, giving

$$\begin{aligned} \frac{\langle N(\text{OVI}) \rangle}{\langle N(\text{OVII}) \rangle} &= \frac{f(\text{OVI})(T = 10^6 \text{ K})}{f(\text{OVII})(T = 10^6 \text{ K})} \\ &= 0.0035, \end{aligned} \tag{4}$$

which is shown as the dashed line in the bottom panel of Figure 16. Admittedly, our approaches to estimate the column density ratios are quite simplistic. Nevertheless, we think

they capture some of the essential underlying relationships between O VI-bearing gas and O VII-bearing gas in the collisional ionization dominated regime and it is reassuring that they are consistent with detailed calculations. Note that at  $N(\text{OVII}) < 10^{15} \text{cm}^{-2}$  photoionization becomes important, especially for related O VI lines, hence our simple physical illustration breaks down in that regime.

#### 4. Conclusions

Utilizing high resolution ( $0.46h^{-1} \text{kpc}$ ), adaptive mesh-refinement Eulerian cosmological hydrodynamic simulations we examine properties of O VI and O VII absorbers in the warm-hot intergalactic medium (WHIM) at  $z = 0$ , along with a physical examination. We find that our new high resolution simulations are in broad agreement with all other simulations with respect to the thermal distribution of baryons in the present universe. In particular, we find that about 40% of the intergalactic medium is in the WHIM. We find that our simulations are in excellent agreement with observed properties of O VI absorbers, including line incidence rate, Doppler width-column density relation, and consistent with observed Doppler width-temperature relation. Physical properties of O VI and O VII absorbers are given, including inter-relations between metallicity, temperature, density, Doppler width, to facilitate a coherent understanding. We highlight some of the important or new findings.

(1) We find that strong O VI absorbers are predominantly collisionally ionized, whereas for weaker absorbers the contributions from photoionization become progressively more important. We find that (39%, 43%, 61%) of O VI absorbers in the column density ranges of  $\log N(\text{OVI}) \text{cm}^2 = (12.5 - 13, 13 - 14, > 14)$  have temperature greater than  $10^5 \text{K}$ . This may be contrasted with the results of Oppenheimer & Davé (2009) where low temperature ( $\sim 10^4 \text{K}$ ), high metallicity, photoionized O VI absorbers dominate even at high column densities ( $\log N(\text{OVI}) \text{cm}^2 > 14$ ). We concur that lack of metal mixing in SPH simulations, which in turn causes overcooling of high-metallicity feedback SPH particles, most severely in high density regions, may be able to account for the discrepancy. We suggest that cross correlations between strong [ $N(\text{OVI}) \geq 10^{14} \text{cm}^{-2}$ ] O VI absorbers and galaxies on  $\sim 100 \text{kpc}$  scales may be able to differentiate between the models.

(2) Velocity structures within absorbing regions are a significant, and for large Doppler width clouds, a dominant contributor to the Doppler widths of both O VI and O VII absorbers. Doppler width is thus a poor indicator of temperature.

(3) Quantitative prediction is made for the presence of broad and shallow O VI lines, which current observations have largely failed to detect. Upcoming observations by COS may be able to provide a test.

(4) The coincidence rates between O VI and O VII lines are found to be small, for

which physical explanations are given. We find that the reported  $3\sigma$  upper limit on the mean column density of coincidental O VII lines at the location of detected O VI lines by Yao et al. (2009) is above the predicted value by a factor of  $2.5 - 4$ , implying that a factor of  $\sim 10$  increase in sample size or sensitivity will be able to yield a definitive detection of O VII column density using the stacking technique even without detection of individual O VII absorbers.

(5) We show that, if the previously claimed observational detection of O VII lines by Nicastro et al. (2005a) is true, our predicted O VII line density is  $2\sigma$  below that. This shows that higher sensitivity X-ray observations of this or other viable targets will be very useful to potentially place strong constraints on the model.

I would like to thank Dr. M.K.R. Joung for help on generating initial conditions for the simulations and running a portion of the simulations and Greg Bryan for help with Enzo code. I would like to thank the referee Mike Shull for critical and constructive reports. I would like to thank Dr. Edward Jenkins for a careful reading of the manuscript and helpful discussion, Dr. Charles Danforth for kindly providing the observational data and useful discussion, Dr. Jeremiah P. Ostriker for useful discussion and Drs. John Wise, Matthew Turk and Cameron Hummels for help with visualization program yt (Turk et al. 2011). Computing resources were in part provided by the NASA High- End Computing (HEC) Program through the NASA Advanced Supercomputing (NAS) Division at Ames Research Center. This work is supported in part by grants NNX08AH31G and NAS8-03060. The simulation data are available from the author upon request.

## REFERENCES

- Bahcall, N. A. 2011, private communications
- Bryan, G. L. 1999, *Comput. Sci. Eng.*, Vol. 1, No. 2, p. 46 - 53, 1, 46
- Bryan, G. L., & Norman, M. L. 1999, in *Structured Adaptive Mesh Refinement Grid Methods*, ed. N. P. C. S. B. Baden (IMA Volumes on Structured Adaptive Mesh Refinement Methods, No. 117), 165
- Buote, D. A., Zappacosta, L., Fang, T., Humphrey, P. J., Gastaldello, F., & Tagliaferri, G. 2009, *ApJ*, 695, 1351
- Cagnoni, I., Nicastro, F., Maraschi, L., Treves, A., & Tavecchio, F. 2004, *ApJ*, 603, 449
- Cen, R. 2012, ArXiv e-prints

- Cen, R., & Chisari, N. E. 2011, *ApJ*, 731, 11
- Cen, R., & Fang, T. 2006, *ApJ*, 650, 573
- Cen, R., Kang, H., Ostriker, J. P., & Ryu, D. 1995, *ApJ*, 451, 436
- Cen, R., Miralda-Escude, J., Ostriker, J. P., & Rauch, M. 1994, *ApJ*, 437, L9
- Cen, R., Nagamine, K., & Ostriker, J. P. 2005, *ApJ*, 635, 86
- Cen, R., & Ostriker, J. P. 1992, *ApJ*, 399, L113
- . 1999, *ApJ*, 514, 1
- . 2006, *ApJ*, 650, 560
- Cen, R., Tripp, T. M., Ostriker, J. P., & Jenkins, E. B. 2001, *ApJ*, 559, L5
- Chen, H.-W., & Mulchaey, J. S. 2009, *ApJ*, 701, 1219
- Cooksey, K. L., Prochaska, J. X., Chen, H.-W., Mulchaey, J. S., & Weiner, B. J. 2008, *ApJ*, 676, 262
- Cowie, L. L., & McKee, C. F. 1977, *ApJ*, 211, 135
- Danforth, C. W., & Shull, J. M. 2005, *ApJ*, 624, 555
- . 2008, *ApJ*, 679, 194
- Danforth, C. W., Shull, J. M., Rosenberg, J. L., & Stocke, J. T. 2006, *ApJ*, 640, 716
- Danforth, C. W., Stocke, J. T., Keeney, B. A., Penton, S. V., Shull, J. M., Yao, Y., & Green, J. C. 2011, *ApJ*, 743, 18
- Danforth, C. W., Stocke, J. T., & Shull, J. M. 2010, *ApJ*, 710, 613
- Davé, R., Cen, R., Ostriker, J. P., Bryan, G. L., Hernquist, L., Katz, N., Weinberg, D. H., Norman, M. L., & O’Shea, B. 2001, *ApJ*, 552, 473
- Davé, R., Finlator, K., & Oppenheimer, B. D. 2011a, *MNRAS*, 416, 1354
- Davé, R., Oppenheimer, B. D., & Finlator, K. 2011b, *MNRAS*, 415, 11
- Davé, R., Oppenheimer, B. D., Katz, N., Kollmeier, J. A., & Weinberg, D. H. 2010, *MNRAS*, 408, 2051
- Fang, T., Buote, D. A., Humphrey, P. J., Canizares, C. R., Zappacosta, L., Maiolino, R., Tagliaferri, G., & Gastaldello, F. 2010, *ApJ*, 714, 1715

- Fang, T., Canizares, C. R., & Yao, Y. 2007, *ApJ*, 670, 992
- Fang, T., Marshall, H. L., Bryan, G. L., & Canizares, C. R. 2001, *ApJ*, 555, 356
- Fang, T., Marshall, H. L., Lee, J. C., Davis, D. S., & Canizares, C. R. 2002, *ApJ*, 572, L127
- Froning, C. S., & Green, J. C. 2009, *Ap&SS*, 320, 181
- Fujimoto, R., Takei, Y., Tamura, T., Mitsuda, K., Yamasaki, N. Y., Shibata, R., Ohashi, T., Ota, N., Audley, M. D., Kelley, R. L., & Kilbourne, C. A. 2004, *PASJ*, 56, L29
- Fukugita, M., Hogan, C. J., & Peebles, P. J. E. 1998, *ApJ*, 503, 518
- Green, J. C., Froning, C. S., Osterman, S., Ebbets, D., Heap, S. H., Leitherer, C., Linsky, J. L., Savage, B. D., Sembach, K., Shull, J. M., Siegmund, O. H. W., Snow, T. P., Spencer, J., Stern, S. A., Stocke, J., Welsh, B., Béland, S., Burgh, E. B., Danforth, C., France, K., Keeney, B., McPhate, J., Penton, S. V., Andrews, J., Brownsberger, K., Morse, J., & Wilkinson, E. 2012, *ApJ*, 744, 60
- Haardt, F., & Madau, P. 2012, *ApJ*, 746, 125
- Heckman, T. M. 2001, in *Astronomical Society of the Pacific Conference Series*, Vol. 240, *Gas and Galaxy Evolution*, ed. J. E. Hibbard, M. Rupen, & J. H. van Gorkom, 345
- Joung, M. R., Cen, R., & Bryan, G. L. 2009, *ApJ*, 692, L1
- Kaastra, J. S., Werner, N., Herder, J. W. A. d., Paerels, F. B. S., de Plaa, J., Rasmussen, A. P., & de Vries, C. P. 2006, *ApJ*, 652, 189
- Komatsu, E., Smith, K. M., Dunkley, J., Bennett, C. L., Gold, B., Hinshaw, G., Jarosik, N., Larson, D., Nolte, M. R., Page, L., Spergel, D. N., Halpern, M., Hill, R. S., Kogut, A., Limon, M., Meyer, S. S., Odegard, N., Tucker, G. S., Weiland, J. L., Wollack, E., & Wright, E. L. 2010, *ArXiv e-prints*
- Mathur, S., Weinberg, D. H., & Chen, X. 2003, *ApJ*, 582, 82
- Narayanan, A., Savage, B. D., Wakker, B. P., Danforth, C. W., Yao, Y., Keeney, B. A., Shull, J. M., Sembach, K. R., Froning, C. S., & Green, J. C. 2011, *ApJ*, 730, 15
- Narayanan, D., Cox, T. J., Hayward, C. C., Younger, J. D., & Hernquist, L. 2009, *MNRAS*, 400, 1919
- Nicastro, F., Mathur, S., Elvis, M., Drake, J., Fang, T., Fruscione, A., Krongold, Y., Marshall, H., Williams, R., & Zezas, A. 2005a, *Nature*, 433, 495

- Nicastro, F., Mathur, S., Elvis, M., Drake, J., Fiore, F., Fang, T., Fruscione, A., Krongold, Y., Marshall, H., & Williams, R. 2005b, *ApJ*, 629, 700
- Oegerle, W. R., Tripp, T. M., Sembach, K. R., Jenkins, E. B., Bowen, D. V., Cowie, L. L., Green, R. F., Kruk, J. W., Savage, B. D., Shull, J. M., & York, D. G. 2000, *ApJ*, 538, L23
- Oppenheimer, B. D., & Davé, R. 2009, *MNRAS*, 395, 1875
- Oppenheimer, B. D., Davé, R., Katz, N., Kollmeier, J. A., & Weinberg, D. H. 2012, *MNRAS*, 420, 829
- O’Shea, B. W., Bryan, G., Bordner, J., Norman, M. L., Abel, T., Harkness, R., & Kritsuk, A. 2005, in *Adaptive Mesh Refinement - Theory and Applications*, ed. T. Plewa, T. Linde, & V. G. Weirs, American Institute of Physics Conference Series, 341
- Persic, M., & Salucci, P. 1992, *MNRAS*, 258, 14P
- Prochaska, J. X., Chen, H.-W., Howk, J. C., Weiner, B. J., & Mulchaey, J. 2004, *ApJ*, 617, 718
- Prochaska, J. X., Weiner, B., Chen, H.-W., Mulchaey, J., & Cooksey, K. 2011, *ApJ*, 740, 91
- Rasmussen, A. P., Kahn, S. M., Paerels, F., Herder, J. W. d., Kaastra, J., & de Vries, C. 2007, *ApJ*, 656, 129
- Savage, B. D., Lehner, N., & Narayanan, A. 2011a, *ApJ*, 743, 180
- Savage, B. D., Lehner, N., Wakker, B. P., Sembach, K. R., & Tripp, T. M. 2005, *ApJ*, 626, 776
- Savage, B. D., Lehner, N., Wakker, B. P., Sembach, K. R., & Tripp, T. M. 2006, in *Astronomical Society of the Pacific Conference Series*, Vol. 348, *Astrophysics in the Far Ultraviolet: Five Years of Discovery with FUSE*, ed. G. Sonneborn, H. W. Moos, & B.-G. Andersson, 363–+
- Savage, B. D., Narayanan, A., Lehner, N., & Wakker, B. P. 2011b, *ApJ*, 731, 14
- Savage, B. D., Narayanan, A., Wakker, B. P., Stocke, J. T., Keeney, B. A., Shull, J. M., Sembach, K. R., Yao, Y., & Green, J. C. 2010, *ApJ*, 719, 1526
- Savage, B. D., Sembach, K. R., Tripp, T. M., & Richter, P. 2002, *ApJ*, 564, 631
- Sembach, K. R., Tripp, T. M., Savage, B. D., & Richter, P. 2004, *ApJS*, 155, 351
- Shen, S., Wadsley, J., & Stinson, G. 2010, *MNRAS*, 407, 1581



- Shull, J. M. 2009, in American Institute of Physics Conference Series, Vol. 1135, American Institute of Physics Conference Series, ed. M. E. van Steenberg, G. Sonneborn, H. W. Moos, & W. P. Blair, 301–308
- Shull, J. M., Roberts, D., Giroux, M. L., Penton, S. V., & Fardal, M. A. 1999, *AJ*, 118, 1450
- Shull, J. M., Smith, B. D., & Danforth, C. W. 2011, ArXiv e-prints
- Smith, B. D., Hallman, E. J., Shull, J. M., & O’Shea, B. W. 2011, *ApJ*, 731, 6
- Springel, V., & Hernquist, L. 2003, *MNRAS*, 339, 289
- Steenbrugge, K. C., Nicastro, F., & Elvis, M. 2006, in ESA Special Publication, Vol. 604, The X-ray Universe 2005, ed. A. Wilson, 751–+
- Stocke, J. T., Penton, S. V., Danforth, C. W., Shull, J. M., Tumlinson, J., & McLin, K. M. 2006, *ApJ*, 641, 217
- Takei, Y., Henry, J. P., Finoguenov, A., Mitsuda, K., Tamura, T., Fujimoto, R., & Briel, U. G. 2007, *ApJ*, 655, 831
- Tepper-García, T., Richter, P., Schaye, J., Booth, C. M., Dalla Vecchia, C., Theuns, T., & Wiersma, R. P. C. 2011, *MNRAS*, 413, 190
- Thom, C., & Chen, H.-W. 2008a, *ApJS*, 179, 37
- . 2008b, *ApJ*, 683, 22
- Tonnesen, S., & Cen, R. 2011, ArXiv e-prints
- Tornatore, L., Borgani, S., Viel, M., & Springel, V. 2010, *MNRAS*, 402, 1911
- Tripp, T. M., Meiring, J. D., Prochaska, J. X., Willmer, C. N. A., Howk, J. C., Werk, J. K., Jenkins, E. B., Bowen, D. V., Lehner, N., Sembach, K. R., Thom, C., & Tumlinson, J. 2011, ArXiv e-prints
- Tripp, T. M., & Savage, B. D. 2000, *ApJ*, 542, 42
- Tripp, T. M., Savage, B. D., & Jenkins, E. B. 2000, *ApJ*, 534, L1
- Tripp, T. M., Sembach, K. R., Bowen, D. V., Savage, B. D., Jenkins, E. B., Lehner, N., & Richter, P. 2008, *ApJS*, 177, 39
- Turk, M. J., Smith, B. D., Oishi, J. S., Skory, S., Skillman, S. W., Abel, T., & Norman, M. L. 2011, *ApJS*, 192, 9

- Werner, N., Finoguenov, A., Kaastra, J. S., Simionescu, A., Dietrich, J. P., Vink, J., & Böhringer, H. 2008, *A&A*, 482, L29
- Wiersma, R. P. C., Schaye, J., & Smith, B. D. 2009, *MNRAS*, 393, 99
- Williams, R. J., Mathur, S., Nicastro, F., & Elvis, M. 2006, *ApJ*, 642, L95
- . 2007, *ApJ*, 665, 247
- Williams, R. J., Mulchaey, J. S., Kollmeier, J. A., & Cox, T. J. 2010, *ApJ*, 724, L25
- Yao, Y., Shull, J. M., Wang, Q. D., & Cash, W. 2012, *ApJ*, 746, 166
- Yao, Y., Tripp, T. M., Wang, Q. D., Danforth, C. W., Canizares, C. R., Shull, J. M., Marshall, H. L., & Song, L. 2009, *ApJ*, 697, 1784